LAMINAR-FLOW WIND TUNNEL EXPERIMENTS

William D. Harvey, Charles D. Harris,
William G. Sewall, and John P. Stack
NASA Langley Research Center
Hampton, Virginia

SUMMARY

Although most of the laminar flow airfoils recently developed at the NASA Langley Research Center have been intended for general aviation applications, new low-drag airfoils have been designed for transonic speeds and wind tunnel performance tested. The objective was to extend the technology of laminar flow to higher Mach and Reynolds numbers and to swept leading edge wings representative of transport aircraft to achieve lower drag and significantly improved operation costs. This research involves stabilizing the laminar boundary layer through geometric shaping (Natural Laminar Flow, NLF) and active control involving the removal of a portion of the laminar boundary layer (Laminar-Flow Control, LFC), either through discrete slots or perforated surface. Results show that extensive regions of laminar flow with large reductions in skin friction drag can be maintained through the application of passive NLF boundary-layer control technologies to unswept transonic wings. An even greater extent of laminar flow and reduction in the total drag level can be obtained on a swept supercritical airfoil with active boundary-layer control.

INTRODUCTION

Long-range market forecasts, operating costs, and strong competition among the airlines have provided incentives for the development of new commercial transport aircraft with substantially improved fuel consumption and operating costs (ref 1). One method of improving fuel consumption is through new laminar-flow technologies and advanced theories in aerodynamics (refs. 2-4), whereby drag reductions are made possible by extending and maintaining laminar boundary layers on wing surfaces, thus reducing skin friction drag. The most direct technique for maintaining a laminar boundary layer is through the passive, or natural laminar-flow (NFL) approach which utilizes favorable pressure gradients to avoid Tollmien-Schlicting instability that leads to transition. These favorable pressure gradients are provided by judicious shaping of the airfoil geometry (refs. 5-9). Maintaining laminar flow by favorable pressure gradient alone becomes increasingly more difficult with increasing Reynolds number and wing sweep at transonic speeds; however, and some form of active or laminar-flow control (LFC) may be required (refs. 2-4, 10, 11).

Natural laminar-flow airfoils have been developed and extensively applied in the past on gliders with very low-drag coefficients realized in flight at low-speeds and Reynolds numbers. More recently, carefully designed NASA laminar-flow airfoils for general aviation aircraft have been developed and wind tunnel tested (refs. 6-9, 12-15) with significantly improved performance characteristics at higher Reynolds numbers than those in the past. Several of these new low-drag airfoils have been applied on different general aviation (GA) aircraft. For example, the NLF(1)-0416 is in production on the Swearingin SX-300 and Freedom Master FM-2 aircraft and the NLF(1)-0215F on the NEKO Lancair 210 and Prescott Pusher 200 aircraft (refs. 6, 7). A Cessna 210 aircraft (refs. 16, 17) has been equipped with a full-span glove of the NLF(1)-0414F (refs. 8, 12) over the original wing for flight tests which verified performance predictions. Also, the NLF(1)-0414 has been slightly modified and applied on the prototype CIRRUS VK 30 aircraft for flight certification.

The above airfoils for general aviation application have achieved drag coefficients that are lower than conventional turbulent airfoils used for either GA or transport aircraft, as illustrated in figure 1. The faired curves are measured drag polars for several different airfoils (with flap deflection) at subsonic and transonic speeds for a chord Reynolds number of 6 million. The low-speed turbulent LS(1)-0417 airfoil is discussed in reference 18 and the 11-percent thick supercritical airfoil in reference 19. The drag polars for the NLF(1)-0215F and NLF(1)-0414F airfoils show a low drag coefficient "bucket" over a rather wide range of lift coefficients which is primarily due to the reduction of skin friction through long runs of laminar flow on both the upper and lower surfaces. These long runs of laminar flow were promoted by shaping the pressure distributions to minimize the amplification of local disturbances that influence transition on the forward portion of the airfoil.

Conventional airfoils for transonic aircraft operate at substantially higher Mach numbers, Reynolds numbers, and sweep than general aviation aircraft and are usually designed for fully turbulent boundary layers which result in higher drag values. From figure 1 it can be seen, for example, that the drag obtained on the NLF(1)-0414F airfoil is about 40- to 50-percent lower than either the turbulent low-speed LS(1)-0417 or supercritical airfoil drag over a range of lift coefficients. The challenge then, is to extend the technology of NLF and LFC to higher Mach numbers, Reynolds numbers, and sweep with low drag. The performance verification of such laminar-flow concepts on airfoils at transonic speeds requires wind tunnels with excellent flow quality environments.

This paper presents experimental wind tunnel results and analysis for two advanced NASA laminar-flow airfoils designed for high subsonic and transonic flow conditions.

SYMBOLS

c Wing or airfoil chord

C_d Drag coefficient, $\frac{\text{section drag force}}{q_\infty c}$

C_L Lift coefficient, $\frac{\text{section lift force}}{q_\infty c}$

C_p Pressure coefficient, $\frac{p - p_\infty}{q_\infty}$

C_Q Suction coefficient, $\frac{(\rho w)_w}{(\rho u)_\infty}$

f frequency

M Mach number

N Natural logarithm of ratio of distance amplitude to its value at the neutral stability point

R Reynolds number per unit length, $\frac{\rho U_\infty}{\mu}$

R_c Reynolds number based on chord, $\frac{\rho U_\infty c}{\mu}$

t Thickness

x Chordwise distance measured from leading edge

α Angle of attack

ρ	Density
δ_f	Flap angle
Λ	Sweep angle
μ	Viscosity

Subscripts:

c	Chord
CF	Cross flow
max	Maximum value
min	Minimum value
N	Normal to leading edge
s	Suction
t	Total
tr	Transition
TS	Tollmien-Schlichting
w	Wall or wake
∞	Free stream

LOW-DRAG AIRFOIL TESTING

This section presents a review of the mechanisms which cause transition; comments on the ability to properly simulate flight conditions in a transonic wind tunnel; and discusses recent advances made in diagnostic instrumentation as applied to low-drag airfoil testing.

One of the most important parameters to be determined during performance verification of low-drag airfoils is the location of boundary-layer transition. Equally important, however, is understanding the mechanisms which cause transition. Transition depends on many factors, including Tollmien Schlichting instability (TS), cross-flow instability (CF), attachment line contamination (AL), and Görtler vortices (GV).

The boundary-layer profile in the direction of the external flow is very similar to that of a two-dimensional boundary layer and by a process of receptivity, small disturbance waves (TS) are developed. These small disturbances grow initially through a linear process, followed by a nonlinear growth and breakdown to transition. For unswept wings, TS disturbance waves are the dominant cause of transition and adverse pressure distributions and increasing Reynolds number have a major influence in their growth.

Wind tunnel experiments on swept wings (ref. 10) have shown that transition may occur near the leading edge due to the instability of cross-flow velocity profiles in the boundary layer. Cross-flow (CF) velocity profiles exhibit inflection points near the surface, and boundary-layer stability theory shows that this instability will lead to transition (refs. 20-24). The major parameters that influence cross-flow instability are wing sweep, pressure distribution, and Reynolds numbers.

Spanwise turbulent contamination, induced by instability of the wing-fuselage juncture boundary-layer or leading-edge roughness, can propagate along the leading-edge of swept wings (ref. 25). The occurrence of such a disturbance along the leading-edge attachment line (AL) could result in the entire wing surface boundary layer becoming fully turbulent for attachment line momentum thickness Reynolds numbers exceeding about 150. Attachment line transition is dependent on wing sweep angle, leading-edge radius, Reynolds number, and flow acceleration in and along the attachment line region.

On the lower surfaces of cambered airfoils, Görtler vortices (GV) may develop as a result of a centrifugal instability of the flow over regions of concave surface geometry (refs. 26-29). Such disturbance vortices are counter rotating pairs that lift off the surface and travel streamwise while remaining in the boundary layer. Görtler vortices are normally highly unstable and quickly lead to transition, however, their growth may be damped when traveling from concave to convex curvature regions.

All of these instabilities are very important (refs. 30-32), and particular attention must be given to avoiding these phenomena when designing and performance testing swept laminar-flow airfoils.

LAMINAR-FLOW TESTING IN TRANSONIC WIND TUNNELS

There are certain limitations in transonic test capabilities which must be considered. Since low-drag airfoil testing is fundamentally a boundary-layer

stability problem, the ability to properly simulate flight conditions in a wind tunnel can be strongly affected by Reynolds number scale (ref. 33), environmental disturbance levels (refs. 34-36), model surface conditions (refs. 37-41), and tunnel wall interference (refs. 42-44). Also important are the methods and instrumentation used to measure disturbance levels and boundary-layer transition characteristics.

DIAGNOSTIC INSTRUMENTATION

The test results obtained with any model is a direct function of the test section flow characteristics. Transonic tunnels are, in general, not well calibrated in terms of free-stream dynamic quantities, but pressure, density, and temperature fluctuations are very important flow disturbance sources and must be known to properly evaluate the turbulence levels (ref. 36). Hot-wire anemometers were used to measure mass flow fluctuations from which components of velocity fluctuations ($\tilde{u}$, $\tilde{v}$, $\tilde{w}$) have been derived. The acoustic environment was also measured using either pressure transducers or microphones.

Another type of anemometry consists of individual thin-film sensors, which may be attached directly to the model surface or flush mounted (ref. 45). It operates on principles similar to the hot-wire anemometer and is used to detect transition. The single-type film sensors (ref. 45) have recently been configured in a multiple sensor array (ref. 46) to simultaneously detect separation and reattachment locations or shock-boundary layer phenomena. More details about advancements in instrumentation for transonic testing are presented in reference 47.

Figure 2 shows the locations of individual thin-film sensors which were deposited on the ends of tiny quartz rods and mounted flush with the surface of a model. The sensors were maintained at 80 °C above local recovery temperature by a constant temperature anemometer. The installation technique for the hot-film sensors on this model is given in reference 45. Examples of output RMS voltage traces and their corresponding boundary-layer states are also shown in figure 2. The amplitude of the fluctuating sensor voltages indicates the relative state of the boundary layer based on assigned arbitrary values of intermittency from 1 to 10. The low amplitude dynamic signal indicates the lower shear stress that is representative of a laminar boundary layer (intermittency factor = 1). The higher amplitude dynamic signal indicates the higher shear stress that represents a turbulent boundary layer (intermittency factor = 10). The transitional boundary layer has both the laminar and turbulent type signals (intermittency factor $\simeq$ 3 to 8) , and it is the relative amount of each, or intermittency factor, which indicates the degree of transition.

Figure 3 shows an example of the Multielement Dynamic Shear Stress Sensor (MEDS^3) technique (ref. 47) that was used to detect shock-induced separation on the upper surface of an airfoil at transonic speeds. The MEDS^3 consists of a large number of closely spaced (0.1-inch) individual Nickel films that were vacuum deposited on a thin substrate of thickness 0.000010 inches in a straight line array. The substrate is bonded to the model surface with sensor array oriented streamwise and leads removed at the model spanwise ends. The figure illustrates that shock-induced separation can be clearly detected by the phase reversal phenomenon observed by P. Stack and S. Mangalam (ref. 46) in low-frequency dynamic shear stress signals. When the shear stress fluctuations from adjacent surface thin-film sensors are correlated, a zero phase is observed upstream of the shock (fig. 3(a)). A -180° phase shift is observed across the shock-induced separation

(fig. 3(b)); a +108° phase shift is observed across reattachment (fig. 3(c)); and the signals are again in phase downstream of the shock-induced separation and reattachment (fig. 3(d)).

TRANSONIC FACILITIES

A brief description of the transonic wind tunnels used to obtain the data presented in this paper follows.

8-Foot Transonic Pressure Tunnel

The NASA Langley 8-Foot Transonic Pressure Tunnel (8-Ft. TPT) is a closed-circuit single-return variable density continuous-flow wind tunnel with a contraction ratio of 20:1. The test section walls are slotted (5-percent porosity) top and bottom, with solid sidewalls fitted with windows for schlieren flow visualization. In 1981, the facility was modified for flow quality improvements and reconfigured for testing of a large-chord swept laminar-flow control (LFC) airfoil at transonic speeds (refs. 11, 48). A honeycomb and five screens were installed in the settling chamber to suppress the disturbance levels in the test section. A contoured liner was installed on all four walls of the test section to simulate free-air streamlines about an infinite yawed wing. This contoured liner produces a contraction ratio of 25:1 and covers the floor and ceiling slots. An adjustable sonic throat ($0.78 \leq M_\infty \leq 0.84$) is located at the end of the test section to block upstream propagation of diffuser noise. The honeycomb and screens were installed as permanent additions to the facility and the liner as a temporary addition, to be removed at the end of the LFC experiment (ref. 48).

The combination of honeycomb, screens, and choke provide very low disturbance levels of $\tilde{p}/p_\infty$ and $\tilde{u}/u_\infty \approx 0.055$ percent, in the test section at $M_\infty \approx 0.8$ and $R/ft \approx 3 \times 10^6$, based on conventional single hot-wire measurements and data reduction techniques. However, results also obtained using a new and more accurate three-wire, hot-wire probe technique at the same test conditions indicated a disturbance level of $\tilde{u}/u_\infty \approx 0.3$ percent (ref. 47).

OHIO STATE UNIVERSITY 6- BY 22-INCH TRANSONIC TUNNEL (6 x 22 TT)

The Ohio State University 6- by 22-Inch Transonic Tunnel is a closed-circuit blowdown type facility (ref. 49). The test section is 6-inches wide and 22-inches high, has plane parallel sidewalls, perforated walls on the top and bottom with separate, self-aspirated plenums, and an array of bars in the exhaust to choke the flow and fix the test section Mach number.

Air is supplied from a 1500 cubic foot storage tank at 2600 psi through two preset control valves, enters the settling chamber through a distribution device and a perforated bulkhead, passing through a honeycomb and six screens, and enters the test section through a three-stage contraction region. Models are mounted in a circular sidewall port, which may be rotated for angle-of-attack from 0° to ±180°. Model pressure distributions are acquired by scanivalves, and Kulite gages are used for diagnostic testing. Wake profiles for the determination of drag are acquired by means of a single traversing probe at transonic speeds or by multiple probes at low speeds.

The maximum stagnation pressure is 4.423 atmospheres with a Mach number range from 0.2 to 1.1. The operational unit Reynolds number range is dependent upon Mach number. For example,

M	R/ft
0.2	2 to 7 x 10^6
.4	4 to 14 x 10^6
.8	7 to 23 x 10^6

RESULTS AND DISCUSSION

Unswept High-Speed NLF Airfoils

High subsonic cruise speeds provide a more difficult design challenge than low subsonic cruise speeds when laminar-flow wings are used. At high speeds, low sweep is desirable to minimize cross-flow boundary-layer instabilities and leading-edge contamination; high sweep is desirable to minimize wave drag and delay transonic drag rise. Consequently, a compromise must be made to prevent boundary-layer instabilities from causing transition near the leading edge and, at the same time, not reduce the drag-rise Mach number to an intolerably low value. Since thinner airfoils rather than reduced sweep are an alternate way of delaying drag rise, airfoil/wing thickness will also be a variable. Another negative factor in high-speed design is the larger Reynolds numbers that are inherent and the adverse effect they have on all instability mechanisms. Careful tailoring of the airfoil contour and the associated pressure distributions is an important activity at low speed but at high speed it is a "make-or-break" one. Favorable gradients required for laminar flow drive the design C_L's down and the wing area up. The need for highly accurate inviscid and viscous flow codes as well as boundary-layer stability routines is clear.

Based on the encouraging results obtained by geometric shaping to achieve extensive laminar flow on both surfaces of the low-speed NLF(1)-0414F airfoil in the wind tunnel (ref. 12) and in-flight (ref. 16), effort has been recently directed towards extension of the concepts to higher speed NLF airfoils. Details of one of the resulting two-dimensional concepts, HSNLF(1)-0213F, are reported in references 13 and 15. Wing body integration of the airfoil is discussed in reference 13 and design of an integrated trailing-edge flap is presented in reference 14.

The HSNLF(1)-0213F, has been fabricated of metal and tested (ref. 15) in the NASA Langley LTPT and 6- by 28-Inch TT to investigate its low-speed high-lift characteristics and high-speed drag-rise characteristics. The airfoil was designed for a lift coefficient of 0.26, Mach number of 0.70, Reynolds number of R_c = 11 x 10^6, and t/c = 0.134. This particular airfoil was designed for application to an essentially unswept wing but could be used for a swept wing as well.

The HSNLF(1)-0213F airfoil profile and design pressure distribution are shown in figure 4. The design shockless pressure distribution was expected to provide laminar flow rearward to about x/c $\simeq$ 0.55 on the upper and x/c = 0.70 on the lower surfaces up to $R_c \leq 10 \times 10^6$. The upper surface forward of 50-percent chord employs the NLF(1)-0414F airfoil geometry; the upper surface aft of the 50-percent chord was modified from that of the NLF(1)-0414F to minimize the possibility of turbulent separation (refs. 2, 13, 15). The bottom side of the nose was slightly modified to minimize off-design pressure peaks on the lower surface. At the same time, the

pressure distribution at the design Mach number and lift coefficient remains essentially subcritical, thereby avoiding recompression shock waves.

Initially, the HSNLF(1)-0213F airfoil was tested both at low speeds ($M \leq 0.3$) and high speeds ($0.35 \leq M \leq 0.80$) and the results are presented in reference 15. Near the design lift coefficient, $0.23 \leq C_L \leq 0.25$, the low-speed tests revealed both low-drag coefficients (0.0038) and transition locations with individual surface thin-film sensors at $x/c = 0.50$ on the upper surface and $x/c = 0.60$ on the lower surface. However, at the design Mach and Reynolds numbers, the high-speed test showed much higher drag coefficients (0.0078 to 0.0083) at the design Mach and Reynolds numbers. This higher drag level was attributed to premature transition caused by poor tunnel flow quality in the NASA Langley 6 x 28 TT.

To investigate the laminar-flow potential of the HSNLF(1)-0213F airfoil, another wind tunnel test was conducted on the same metal model that was used in the NASA Langley 6 x 28 TT, with multielement thin-film sensors to detect transition, separation, reattachment, and shock location (ref. 46). The 6- by 22-inch transonic wind tunnel at the Ohio State University (ref. 49) was used for this experiment. Test requirements and facility capabilities limited the maximum chord Reynolds numbers to 5.0 million. Limited test results were also obtained on a composite model in this same facility.

Some of the results from this experiment are shown in figures 5 and 6, where comparisons have been made between the experimental and theoretical pressure distributions. Included with the pressure distributions are the locations for the beginning, peak, and end of transition as indicated by the thin-film sensors on the model's upper surface that extend from $0.3 \leq x/c \leq 1.0$. The theory (ref. 50) has no laminar boundary layer; the start of the turbulent boundary layer was arbitrarily set at 0.40c on the upper and 0.50c on the lower surfaces.

The shock-free experimental and theoretical pressure distributions presented in figure 5, at the design Mach number and lift coefficient agree very well up to the recompression zone for both the upper and lower surfaces. The theory then shows a stronger pressure recovery than the experiment. Good agreement exists between the measured and predicted drag of $C_d \approx 0.0057$. No wall interference corrections were made to the experimental data.

The hot-film sensors (refs. 46, 47) on the upper surface indicate the beginning of transition at $x/c = 0.50$, near minimum pressure, followed rapidly by peak transition at $x/c = 0.545$, then fully turbulent flow developing at $x/c = 0.593$. No boundary-layer separation was indicated by these upper surface sensors. It should be noted that, while the measured transition location agrees with the design objective, the results are limited to a Reynolds number of 4.2 million instead of the design 11 million.

Figure 6 shows another experimental and theoretical pressure distribution comparison at an off-design Mach number of 0.77 which results in a strong shock wave on the upper surface, as indicated by both experiment and theory (ref. 50). However, the experiment shows that the beginning of the shock is approximately 0.10c ahead of the theoretical location, along with significantly reduced suction levels, followed by an entirely different pressure distribution than shown by theory. It should be noted that the theory (ref. 50) has no provision for shock-boundary layer

interaction, and there were no wall interference corrections made to the data. Thin-film sensors in the region of the shock wave indicated an attached laminar separation bubble just downstream of the beginning of transition, which occurred at the shock wave itself (fig. 3). Therefore, the laminar boundary layer extends rearward to the shock wave which interacts with a laminar separation bubble and causes it to shift forward. The experimental pressure distribution following the separation bubble, i.e., after the reattachment point, develops a positive gradient.

Figure 6 not only shows large differences between measured and predicted pressure distributions, but also between drag coefficients that are caused by interaction of the laminar boundary layer and shock wave that are not accountable by the theory. For the design case (fig. 5), good agreement exists between theoretical predictions of pressure distribution and drag since there is no shock or boundary-layer separation.

Figure 7 shows a comparison of the transonic drag-rise with increasing Mach number obtained on the same metal model of the HSNLF(1)-0213F airfoil in two wind tunnels. Also shown for comparison is a single-drag value at M = .7 obtained on a composite model of the HSNLF(1)-0213F in the O.S.U. 6 x 22 TT. The angle of attack was set at zero and the resulting lift coefficients ranged from 0.26 to 0.28. From figure 7, it appears that measured and predicted low to moderate drag coefficients (fig. 5), ranging from about 0.0057 to 0.0065, can be attained on the metal model up to a Mach number of 0.73 at $R_c = 4.2 \times 10^6$. Apparently, much lower drag values of about 0.0045 are possible at the design M = 0.7 with the smooth composite model compared to that obtained for the metal model in the same tunnel. With transition fixed at 0.05 chord, the drag coefficient increases to 0.0083 while the drag-rise Mach number is reduced to about 0.715.

SWEPT SUPERCRITICAL LFC AIRFOILS

The concept of combining geometric shaping and boundary-layer control through suction on airfoils to achieve very low drag dates back to the late 1930's when the feasibility of achieving full-chord laminar flow on conventional swept wings, with suction applied through many closely spaced surface slots, was established by Pfenninger (refs. 10, 51). Results were obtained on large-chord wing sections (modified NACA-66012) of 30° sweep and t/c = 0.12 in three different wind tunnels (ref. 10) and flight (refs. 37, 39). Flight tests on the X-21 and F-94 aircraft (refs. 52, 53) achieved full-chord laminar flow to $R_c = 22 \times 10^6$ at $M_\infty = 0.80$ and $R_c = 36 \times 10^6$ at $M_\infty = 0.72$, respectively. The X-21 wing was swept 33° and the F-94 wing was unswept. Since this research demonstrated the potential for significant drag reduction through application of boundary-layer control, interest was generated in evaluating the feasibility of combining boundary-layer control with supercritical airfoil technology at conditions which are typical of high-performance transports. About 1975, Dr. Werner Pfenninger proposed such an experiment and a large chord swept supercritical airfoil, with suction capability on both the upper and lower surfaces, was designed, constructed, and tested in the NASA Langley 8-Ft. TPT (fig. 8). This NASA airfoil is designated SCLFC(1)-0513F. Details of the airfoil and suction system design along with the test setup have been reported (ref. 11). One of the major objectives of the experiment was to evaluate the feasibility of slotted and perforated suction surface concepts for laminarization in a large supercritical zone.

As mentioned above, requirements for this test included modification of the wind tunnel to achieve the desired flow quality and test section wall contouring to simulate free air flow about an infinitely yawed model at the design Mach number (refs. 44, 48).

Slotted and Perforated Models

The LFC airfoil model has an aspect of about 1.0. It consists of a wingbox structure to which three upper and three lower surface suction panels and a trailing-edge flap are attached (fig. 9). Figure 10 is a sketch showing the slotted suction surface with the internal airflow metering and ducting system. Laminar flow control by boundary-layer removal on the slotted configuration was achieved with suction through closely-spaced spanwise slots (fig. 10) on the airfoil surface. After passing through the slots and small underlying plenums, the air passed through appropriately spaced metering holes and was collected by spanwise ducts of constant cross section with suction nozzles located at the ends. Air from the nozzles passed through model evacuation lines, through airflow control boxes which controlled the amount of suction to the individual duct nozzles, through variable nozzles, through hoses to a collector manifold and, finally, to a 10,000 CFM compressor with a 4.5:1 compression ratio which supplied the suction.

In the upper surface midspan region where full-chord laminar flow was expected, the suction slots extended rearward onto the flap to x/c = .96. On the lower surface, suction extended rearward to x/c = .84. Outside of the laminar midspan region, the upper surface spanwise slots extend rearward only to the flap hinge line at x/c = .89. A photograph of the swept LFC airfoil installed in the test section of the 8-Ft. TPT is shown in figure 11. Figure 11(a) is a downstream view looking at the swept leading-edge upper surface, and figure 11(b) is an upstream view of the trailing edge. Suction ducts to control the boundary layer in the model/tunnel junctures may be seen in the liner at the floor and ceiling (fig. 11(a)).

Figure 12 is a sketch of the swept LFC airfoil model illustrating replacement of the slotted upper surface with three perforated suction surface panels. The perforated panels were designed and fabricated by McDonnell Douglas Aircraft Company under contract to the NASA Langley ACEE Project Office (ref. 54). The original bottom surface slotted panels were retained for this configuration. Figure 13 is a sketch showing the perforated suction surface and internal airflow metering and ducting system. This surface was fabricated with fiberglass flutes or hat sections with a continuous perforated skin bonded to the outer part of the hat sections resulting in alternating suction and nonsuction areas. These areas extend spanwise and are constant in width. The active suction and nonsuction area widths are nominally 0.60-in. and 0.3-in. wide, respectively. The perforations in the surface skin, produced by electron beam drilling, are approximately 0.0025 inches in diameter on 0.025-inch spacing, yielding an open area porosity ratio of 0.8 percent. Beneath each suction strip are spanwise flutes and ducts that are connected through a number of metering holes. Calibrated suction nozzles are provided in each duct and are connected via hoses to the suction compressor through the same control used for the slotted model. The perforated suction surface extends from $0.02 \leq x/c \leq 0.89$ along the entire span. The turbulent wedge regions at the ends of the model are very similar to those for the slotted model and the suction applied and controlled is also similar.

Experimental Results

Figures 14 and 15 show a comparison of the measured and theoretical chordwise pressure distributions at midspan and $M_{design} = 0.82$ for chord Reynolds numbers of 10 and 20 x 10^6. Figure 14 shows the measured pressure distribution for the slotted model to be essentially shock free at $R_c = 10 \times 10^6$ with full-chord laminar flow (as evidenced by the surface thin-film gages used for detecting transition) on both upper and lower surfaces (see figs. 16, 17). The higher and less uniform than design velocities on the upper surface were attributed to classical problems associated with wind tunnel testing--model deformation and wall interference. Local Mach numbers measured on the test section wall opposite the upper surface indicate that the supersonic bubble on the airfoil was larger than design and extended practically to the wall. The larger bubble was believed to be due to the inability to account for three-dimensional boundary-layer displacement thickness effects with the accuracy desired in the design analysis of the contoured liner wall (ref. 44).

The pressure distribution for the perforated model at $R_c = 10 \times 10^6$ (fig. 14) is very similar to that of the slotted model except for slightly higher velocities on the upper surface and with a very weak shock appearing at about x/c = 0.70. Even with the higher velocities and weak shock on the perforated upper surface, full-chord laminar flow was achieved (fig. 18) for $R_c = 10 \times 10^6$. These higher upper surface velocities are related to the more positive 0.71° angle of attack required for the perforated model as compared to the 0.51° angle of attack for the slotted model. The higher angle of attack was required to minimize the strength of the shock at the end of the supersonic zone as discussed below.

Measurements under simulated loading conditions indicated that the perforated model deformed more in the chordwise direction than the slotted model. Because of the larger deformation, the rear panel of the perforated model was closer to the test section wall opposite the upper surface than was the slotted model when both were positioned at $\alpha = 0.51°$. This resulted in a saddle back shaped upper surface pressure distribution with a strong shock near x/c = 0.70 and a sonic bubble which impinged on the wall. Since the angle of attack was adjusted by rotating the model about x/c = 0.24, increasing the angle moved the trailing edge of the model away from the wall, weakening the upper surface shock and reducing the extent of the sonic bubble.

In order to reduce the velocities nearer to design, it was necessary to modify the perforated model mounting blocks and translate the model 0.25-inch further from the wall above the upper surface. With this translation, the angle of attack could be reduced to 0.71° without strengthening the upper surface shock. At these conditions, the upper surface pressure was very near that for the slotted model and the extent of the sonic bubble was about the same for the two models.

With increases in Reynolds number, transition moved forward gradually on the upper surface and rapidly on the lower surface (figs. 16-18). Figure 15 compares the resulting pressure distributions at $R_c = 20 \times 10^6$ and indicates very similar distributions for the two models except for the previously mentioned higher velocities on the upper surface of the perforated model and the tendency for the perforated model to show a developing shock on the lower surface near midchord. The laminar boundary layer on the lower surface (both models used the same three slotted lower surface panels, fig. 9) was unable to withstand the adverse pressure gradient

leading into the trailing edge cusp region above approximately $R_c = 14 \times 10^6$ where transition moved rapidly forward and the flow separated in the rear cusp. With decreasing extents of laminar boundary layer and the appearance of separation on the lower surface, the local effective area distribution of the test section changes, resulting in higher free-stream Mach numbers being required to achieve the design plateau pressure distribution as Reynolds number increased. A loss in model lift and increase in drag also occur with decreasing extents of laminar flow.

It should be noted that, in general, as the free-stream Mach number increases, the corresponding static pressure decreases rapidly, causing the local differential pressure drop across a given suction surface to become large with corresponding increased suction requirements. This trend may become a challenge for designers of high transonic-supersonic LFC transports.

Analysis of spanwise pressure distributions and transition patterns at M_{design} showed that the flow was nearly two dimensional over the slotted and perforated models but that the leading edge peak pressure coefficient tended to vary along the span. In addition, transition tended to move forward with increases in Reynolds number in a somewhat non two-dimensional fashion. In general, transition tended to be more rearward toward the ceiling where leading-edge pressure peaks were lowest, and more forward toward the floor where they were higher.

The measured and theoretical suction coefficient ($C_Q = \frac{(\rho w)_w}{(\rho u)_\infty}$) distributions required to maintain full-chord laminar flow over both the slotted and perforated upper surfaces at $M_{design} = 0.82$ and $R_c = 10 \times 10^6$ are shown in figure 19. The design suction requirements were based on shock-free flow and minimum level required to maintain laminar flow. The measured suction required for full-chord laminar flow on the slotted model was higher than that predicted, in some cases by as much as 50 percent, and generally represents the maximum suction capability of the system. The measured suction requirements on the perforated model were much higher than on the slotted, particularly over the seven suction ducts on the forward panel ($x/c < 0.26$). The relative magnitude of the measured suction requirements over the next five suction ducts on the center panel ($0.26 < x/c < 0.59$) varies somewhat, but over the remaining nine suction ducts on the aft panel ($x/c > 0.59$), the available suction capability of the perforated panel was much lower than that theoretically required or that available on the slotted model. The measured suction distribution over the aft panel of the perforated model represents the maximum suction capability of the panel as designed and installed. The measured suction distribution over the forward and center panels represents the maximum suction available after extensive hardware modification has been made to increase their suction capability. These modifications include enlarging all metering holes in the flutes (fig. 13) in the two panels, enlarging the laminar nozzle extensions in the two panels, and adding a second suction nozzle to each laminar duct in the forward panel.

There was, of course, an infinite combination of individual duct suction levels and overall suction distribution possibilities. The distributions shown (fig. 19) consist, in general, of the maximum suction capability of each suction duct combined with the maximum suction capacity of the compressor system used to provide suction to the model. Small local variations may be permissible within these overall distributions without an adverse effect on the extent of laminar flow within the resolution permitted by the chordwise spacing of thin films. (See fig. 2). Reductions in the overall suction level of the distributions, by varying compressor

controls in amounts large enough for the sum of the suction drag over the entire upper surface to be measurably different, generally resulted in either a detrimental effect on the laminar-flow pattern (transition behavior) or an increase in wake drag. The higher than theoretically predicted suction requirements on the upper surface of both models are attributed to uneven velocities/pressures on the upper surface discussed above and the wind tunnel environment.

The higher suction requirements on the forward region of the perforated model compared to the slotted model was attributed to several factors. These factors include the less rigid construction of the perforated panels and the resulting greater, and more uneven, deformation under load; the waviness of the perforated surface, some of which is associated with the corrugated substructure, is also greater than on the slotted panels.

Since the lower slotted suction surface was the same for either the slotted or perforated model upper surfaces, an example comparison between the measured and predicted suction is shown in figure 20 for M = .82 and R_c = 10 x 10^6. The measured higher than predicted suction requirements are attributed to the suction control required for the minimization of centrifugal Görtler type boundary-layer instabilities and interactions with cross flow in the concave regions of the lower surface (fig. 8).

The contributions to the total section drag coefficient for the slotted LFC airfoil at M_∞ = 0.82 are shown in figure 21 over a chord Reynolds number range of 10 to 20 million. The division of suction drag contributions between the upper or lower surfaces may be made since the suction drag is computed duct-by-duct and integrated over each surface independently. The wake drag is separated into upper and lower surface components on the basis of the assumption that the wake can be divided between the upper- and lower-surface at the point on the wake rake where the stagnation pressure loss is the greatest. The data (fig. 21) indicate that the larger contribution to the total drag is from the lower surface. With full-chord laminar flow over the upper and lower surfaces for $R_c \leq 12 \times 10^6$, the contribution to the total drag was about 1/3 due to wake and 2/3 due to suction drag. The sharp rise in wake drag on the lower surface between 14 and 15 million Reynolds number is associated with rapid forward movement of transition (fig. 17) and separation of the boundary layer in the lower aft cusp. The contribution of the suction drag is about 40 percent for the upper and 60 percent for the unconventional lower surface (fig. 21).

Wind tunnel tests have been conducted earlier on several swept LFC airfoils at low speeds (refs. 10, 51) with extensive laminar flow and low drag. These airfoils had suction applied only on the upper surface. Figure 22 shows the upper-surface pressure distributions and minimum total drag measured at the design lift condition (C_L = .3) on two earlier low-speed LFC airfoils of different sweep as compared to the present supercritical LFC airfoil with C_L = .55. The low-speed LFC designs, based on standard NACA airfoil profiles, have favorable pressure gradients over the first 50 percent or more of the chord, and much less severe adverse pressure gradients aft, than the supercritical design. The higher design C_L of the SCLFC(1)-0513F airfoil does not permit a long run of favorable pressure graident. Figure 22 shows only the upper-surface measured minimum profile drag coefficients corresponding to the upper-surface pressure distributions at R_c = 10 x 10^6. As might be expected, the supercritical design has a somewhat larger suction drag penalty than the NORAIR model, which has the greatest extent of favorable pressure gradient (fig. 22), and only a slightly larger suction drag penalty than the

University of Michigan 5- by 7-Foot Tunnel model, while the wake drag contribution is about the same in all cases. An increase in wake drag for $M_\infty \approx 0.70$ is observed on the slotted LFC airfoil (fig. 22) and attributed to the formation of a weak shock wave near the leading-edge as the supersonic bubble begins to develop. As the bubble develops near the leading edge ($0.78 < M_\infty < 0.80$), full-chord laminar flow still exists, but periodic turbulent bursts occur over the upper surface causing an increase in wake drag. It may be concluded that the basic phenomenon of applying suction laminarization over an extensive supercritical zone with full-chord laminar flow at $R_c = 10 \times 10^6$ is feasible as demonstrated on a swept LFC airfoil at high lift conditions. It is clear, however, that the "nonideal" transonic wind tunnel test environment (refs. 42, 44) and surface waviness (refs. 40, 41) do cause a loss in the amount of laminar flow achieved. Consequently, the data obtained are conservative; i.e., one should do better in flight.

Figure 23 shows the in-flight upper surface wing and glove pressure distributions for the X-21 and F-94 aircraft compared with that measured on the SCLFC(1)-0513F airfoil. Full-chord laminar flow was achieved for each experiment and conditions shown. The present wind tunnel model has not only a larger local Mach number but extent of sonic zone than the flight (refs. 52, 53) results, and also has a much higher lift coefficient. The X-21 wing and F-94 glove have favorable pressure gradients in the nose region and much less severe adverse gradients in the aft region than the supercritical airfoil.

Figure 24 shows a comparison of the drag measured on the upper surface of these three configurations. With full-chord laminar flow on the present model for $R_c \leq 12 \times 10^6$, the total drag level was about the same as that measured in flight on the X-21 or F-94. Detailed suction drag measurements were not determined in flight on the X-21, but an estimate of the total drag was made from reference 55. The higher total drag measured for the present LFC airfoil for $R_c \geq 12 \times 10^6$ was discussed earlier and is attributed mainly to the surface deformation, waviness, and the wind tunnel environment. However, the indicated drag level for the upper surface of the SCLFC(1)-0513F airfoil, obtained with full-chord laminar flow, is about one-third that of the upper surface of a conventional turbulent airfoil.

High-Speed HLFC Airfoils

Another and more practical concept for obtaining long runs of laminar flow at high Mach number is a hybrid configuration which would combine suction over forward regions of the upper surface with natural laminar-flow (NLF) concepts over rearward regions (refs. 2, 3). An attempt was made to simulate such hybrid laminar-flow control (HLFC) conditions during the 8-Ft TPT LFC experiment by turning off suction over regions of the upper surface. On the lower surface, suction was maintained for $0 \leq x/c \leq 0.25$ to control the flow between the lower surface and tunnel wall. This simulation of HLFC involved first establishing laminar flow to the most rearward location, then progressively turning off upper surface suction starting with the most rearward suction duct and measuring the extent of laminar flow that was maintained downstream of the turn-off points. The variation of transition location on the upper surface with chordwise extent of suction is shown in figure 25 for $M_\infty = 0.82$ and two chord Reynolds numbers. The results indicate that laminar flow could be maintained well beyond termination of suction. With no suction, laminar flow was present back to about 15- and 25-percent chord, depending on R_c. At $R_c = 10 \times 10^6$, the measured total drag was $C_d \approx 0.0012$ with $0 \leq (x/c)_{suction} \leq 0.96$ and increased to $C_d \approx 0.0025$ with no suction. The C_{dw} contribution increases and

becomes a larger fraction of $C_{d_{total}}$ as suction is reduced to zero. Clearly, this simulated HLFC approach must be considered somewhat "nonidealistic" and the results conservative since no effort was made to seal or smooth the unsucked regions of the airfoil. Furthermore, the pressure distributions (figs. 14 and 15) are not like that which would be designed for an HLFC configuration.

Almost any form of LFC could be considered a hybrid configuration, since, from a practical standpoint, one would probably not apply suction control over the full chord on both surfaces. Furthermore, considerable research is required to establish the effectiveness of suction control through shock boundary-layer interaction regions that occur at off-design conditions. Thus, the attractiveness of a form of HLFC that requires limited suction control in the leading-edge region for cross-flow instability followed by a favorable pressure gradient to maintain attached laminar flow (as far rearward as possible) is substantial. This concept would provide the maximum drag reduction with minimum suction requirements and complexity at design and off-design transonic speeds.

NASA Langley has designed, fabricated, and is currently installing an HLFC airfoil in the 8-Ft TPT for testing. The HLFC concept was originated by P. J. Bobbitt and the design was carried out by S. H. Goradia and J. C. Ferris and is reported in reference 56. It should be noted that constraints were placed on the HLFC design that required utilization of the present LFC airfoil and liner configurations in order to minimize costs and schedules for fabrication and testing. Only the upper mid and aft model surface regions ($0.25 \leq x/c \leq 1.0$) were altered in order to achieve a somewhat favorable pressure gradient downstream of suction turn off. The upper forward perforated and lower three-slotted surface panels were retained (figs. 9, 12). A new flap was designed and required to match the new upper aft surface camber change.

Figure 26 shows the HLFC airfoil design upper surface pressure and suction distribution for $M_\infty = 0.81$, $C_L = 0.47$, $R_c = 15 \times 10^6$ and sweep angle of 23°. Suction control is applied from $0.025 \leq x/c \leq 0.26$ through the original perforated panel for the HLFC concept. The HLFC type pressure distribution yields somewhat less lift than that for LFC in an effort to avoid shocks and aft separation. Predicted drag coefficients (fig. 27) for the upper surface of the HLFC airfoil are expected to be on the order of two times the drag levels for the full-chord laminar-flow shockless LFC airfoil for $R_c < 12 \times 10^6$.

DRAG REDUCTION SUMMARY

Figure 28 is an attempt to summarize the drag reduction achieved for the HSNLF(1)-0213F and SCLFC(1)-0513F airfoils designed for transonic operation, compared with several other recent NASA laminar-flow airfoils developed for low speeds shown as a hatched region in the figure. The results shown are for the minimum total drag measured which includes both wake and suction drag. The symbols are for drag values measured on these airfoils with extensive laminar flow over the upper and lower surfaces compared to fully turbulent flow conditions on airfoils as also indicated by hatched band. The values shown correspond to the minimum drag levels measured with α and $\delta_f = 0°$ but for different R_c's. The data (fig. 28) indicate that an average drag value of about 0.0085 exists when the flow is turbulent and $M_\infty \cos \Lambda \leq 0.75$ and about 0.0035 with laminar flow achieved by NLF or LFC. This represents a total drag reduction of about 60 percent that has been achieved and extended to transonic speeds with the new NASA airfoils. Apparently,

the presence of a shock on the unswept HSNLF(1)-0213F airfoil with laminar flow causes wave drag that influences drag rise for $M_\infty \geq 0.7$.

STABILITY METHODS ANALYSIS

Empirical relations, derived from earlier low-speed and Reynolds number experiments, are available and may be used for predicting transition (refs. 57, 58). More sophisticated approaches have been developed to determine the transition location on swept and unswept wings for incompressible (refs. 20, 59) and compressible (refs. 60, 61) flow.

The more sophisticated methods used for design and analysis of the airfoils herein have been described and presented earlier (refs. 20, 59-61). These methods are based on the temporal stability theory for laminar boundary layers where the local amplification rates are obtained as solutions of the governing Orr-Sommerfeld equation as functions of the frequency, wavelength, and orientation angle of the disturbance. If it is assumed that a disturbance has an initial amplitude A_o at some location X_o in the boundary layer, then the amplification ratio A/A_o at any downstream point X can be calculated. This amplification ratio can be expressed as an exponential function e^N where N is referred to as the amplification exponent or N-factor. N-factors may be related to the growth of disturbance amplitudes and used, based on experience, to predict transition conditions. These analysis methods only apply in linear attached flow regions and calculations must be carried out to the extent that the amplification exponent N becomes a maximum for all frequencies. When using the N-factor method for design, one is left with the arbitrary or empirical choice of a limiting N-value for transition. When used for analysis, limiting N-values are determined by the experimental transition locations.

Calibration of Stability Codes

A number of computer codes are available to calculate N-factors for Tollmien-Schlichting (TS) waves and cross-flow (CF) vortices. Some examples are the incompressible SALLY (ref. 59) and MARIA (ref. 20) codes and the compressible MACK (ref. 61) and COSAL (ref. 60) codes. The MARIA code is the most straightforward and economical to apply but is restricted to CF calculations only. The SALLY code may be used for CF or TS analysis.

Experimental transition data have been recently obtained and analyzed on NLF and LFC airfoils (refs. 3, 62), on bodies of revolution (ref. 63), in wind tunnels and on wings or gloves in flight (refs. 3, 62, 64-70). The measured pressure profiles and suction distributions from a number of these experiments were used as input to the above mentioned codes to calculate local disturbance growth rates and integrated amplification ratios (N-factors). N-factors calculated at the experimently measured transition locations for both TS and CF disturbances were compared to determine which instability was the most amplified.

Figures 29 and 30 are an attempt to summarize the calculated lowest N-factors at measured transition for TS and CF, respectively. It should be noted that there exists higher referencable N-factor values than shown in the figures; only the lower values were chosen to establish a low N-factor boundary and Mach number trend. In figure 29, calculated N-factors for situations where the TS instabilities dominate (CF negligible) is given; figure 30 is for situations where CF dominates (TS

negligible). The N-factors shown for the NASA NLF(1)-0414 wind tunnel and Cessna 210 flight tests and the NASA SCLFC(1)-0513 wind tunnel tests with slotted suction surface were calculated using the envelope method of solution in the SALLY and COSAL codes, with identical input data for each point (ref. 62). All other results on figures 29 and 30 (refs. 64-70) were calculated using either the SALLY, COSAL, or MACK codes. The incompressible TS N-factors (open symbols) approach a constant lower limit of about N = 9--while those N-factor values obtained with the compressible codes (solid symbols) decrease over the indicated speed range (solid curve) and are about 50 percent lower at $M_\infty \cos \Lambda \approx 0.8$. These trends (fig. 29) are intended to establish a theory calibration of the allowable lower limit for disturbance amplification. The limited number of incompressible CF N-factors (fig. 30) have a minimum value of 9 while those from the compressible code decrease to values of 4 or 5. The results strongly indicate that, on the average, a constant (N = 9) but conservative N-factor value can be used in applying the incompressible codes. However, knowledge of both the conservative trend and level of the N-factor (figs. 29, 30) is required when applying the compressible codes. The consistency of this correlation validates and extends the use of both incompressible and compressible linear stability theory for conservative design to high speeds. The fact that the lower limit of the N-factor trend from the compressible codes decrease with $M_\infty \cos \Lambda$ implies that "compressibility effects" are not conservative in stability analysis; i.e., transition takes place with less amplification than for incompressible flow.

All of the N-factors calculated and presented in figure 29 for the LFC airfoil were based on the beginning of transition location (ref. 62). However, if the transition point is selected further downstream of this location, the incompressible or compressible boundary-layer codes generally predicted laminar separation leading to a very rapid increase in the growth of the N-factor over a very narrow frequency range. This also caused arbitrary selection of amplification factors that could be on the order of twice or more those values shown in figure 29 for the SCLFC(1)-0513F airfoil. Calculated values of N_{TS} along the slotted LFC airfoil chord were found to vary depending upon the chordwise extent of applied suction and accuracy with which transition location could be determined. For example, with laminar flow over less than 30-percent chord on the upper suface, the calculated N_{TS} values were from 8.5 to 17.5 (ref. 62). However, with laminar flow beyond 30-percent chord, the N_{TS} values were found to decrease dramatically below these values to about 1 or 2. Thus, it becomes very important to account for this chordwise variation in N-factor for a given design case. The indicated trends (figs. 29-30) could be attributed to the wind tunnel disturbance environment; however, flight N-factors are shown that agree with the wind tunnel data.

Figure 31 is an attempt to evaluate the influence of transonic wind tunnel turbulence level on the calculated N-factors at transition on models. Shown for comparison are calculated values of N_{TS} on the slotted SCLFC(1)-0513F airfoil in the Langley 8-Ft TPT (ref. 62) and two bodies of revolution in the NASA Ames 12-Ft PWT (ref. 63). Also shown is the empirical relation for the variation of N_{TS} with turbulence level generated by MACK (ref. 71) for $\tilde{u}/u \geq 0.1$ percent. With the exception of a single data point ($N_{TS} = 10.5$), all of the calculated values tend to fall within a horizontal band between N_{TS} values of about 5 to 8 indicating little or no influence of tunnel turbulence level as suggested by references 63 and 71. In fact, the LFC airfoil results shown for $\tilde{u}/u \approx 0.2$ percent ($M_\infty = 0.7$) are for essentially full-chord laminar flow on both surfaces up to $R_c \lesssim 22 \times 10^6$. For $\tilde{u}/u \approx 0.05$ percent ($M_\infty = 0.82$) full-chord laminar flow existed for $R_c = 10^7$ and

$N_{TS} \approx 4.5$ and with $0.2 < (x/c)_{tr} < 0.3$ the $N_{TS} = 7.5$ for $R_c = 2 \times 10^7$. Therefore, the present limited results (figs. 29, 30) suggest the need for further calculations and analysis in order to complete the calibration of compressible boundary-layer stability theories. Note that the $\tilde{u}/u$ values just quoted are for single hot-wire measurements.

CONCLUDING REMARKS

Significant amounts of laminar flow have been achieved through passive (NLF) or active (LFC) methods at high speeds. This has been demonstrated on recently developed low-drag airfoils which use boundary-layer suction control or favorable pressure gradient. Wind tunnel tests of these concepts, from subsonic to transonic speeds, have shown significant improvements in lift-to-drag ratio over previous airfoils.

Natural laminar flow was maintained over 50-percent chord and shock-free conditions on an unswept airfoil designed for high speed and moderate lift. A reduction in the drag of about 40 to 50 percent over turbulent designs was realized. Suction laminarization, through either a slotted or perforated surface, over a large supercritical zone has been shown to be feasible to high-chord Reynolds numbers even under "nonideal" surface and test environment conditions on a swept LFC airfoil at high-lift coefficients. With essentially shock-free flow at $M_\infty = 0.82$, full-chord laminar flow on the upper and lower surface was achieved for $R_c \leq 12 \times 10^6$. As Reynolds number increased above $R_c \geq 12 \times 10^6$, transition moves gradually forward on the upper surface but laminar flow was maintained over most of the supersonic zone on the slotted and perforated surfaces for $M_\infty \approx 0.82$. The extent of suction laminarization was found to be slightly less for the perforated surface than for the slotted surface and attributed to a less rigid model and a more wavy surface. A reduction in the drag level of about 80 percent for the upper surface only and about 60 percent for both upper and lower surfaces was achieved with full-chord LFC.

Calculations using measured wind tunnel and flight data show differences in the trends and the lower bounds of the amplification ratios as calculated by incompressible and compressible linear boundary-layer stability theory. Lower N-factor levels have been obtained from the compressible stability theory than the incompressible; consequently, compressible calculations are not conservative, as previously thought.

REFERENCES

1. Maglieri, Domenic J.; and Dollyhigh, Samuel M.: We have Just Begun to Create Efficient Transport Aircraft. Astronautics and Aeronautics, Feb. 1982, pp. 26-38.

2. Bobbitt, P. J.; Waggoner, E. G.; Harvey, W. D.; and Dagenhart, J. R.: A Faster "Transition" to Laminar Flow. SAE-851855, Oct. 1987.

3. Harvey, W. D.: Boundary-Layer Control for Drag Reduction. SAE-872434, Nov. 1987.

4. Harvey, W. D.; McGhee, R. J.; and Harris, C. D.: Wind Tunnel Testing of Low-Drag Airfoils. NASA CP-2413, Apr. 1985.

5. Abbot, Ira H.; and von Doehhoff, Albert E.: Theory of Wing Sections. New York, Dover Publications, 1959.

6. Somers, Dan M.: Design and Experimental Results for a Natural-Laminar-Flow Airfoil for General Aviation Application. NASA TP-1861, 1981.

7. Somers, Dan M.: Design and Experimental Results for a Flapped Natural-Laminar Flow Airfoil for General Aviation Application. NASA TP-1865, 1981.

8. Viken, J. K.: Aerodynamic Design Considerations and Theoretical Results for a High Reynolds Number Natural Laminar Flow Airfoil. M. S. Thesis, George Washington University, Jan. 1983.

9. Viken, J. K.: Boundary-Layer Stability and Airfoil Design. NASA CP-2413, Apr. 1985.

10. Pfenninger, W.: Special Course on Concepts for Drag Reduction, Chapter 3 - Laminar Flow Control, Laminarization. AGARD Report 654, Jun. 1977.

11. Harris, Charles D.; Harvey, William D.; and Brooks, Cuyler, W.: The NASA Langley Laminar Flow Control Experiment on a Swept, Supercritical Airfoil. NASA TP-2809, 1988.

12. McGhee, R. J.; Viken, J. K.; Pfenninger, W.; Beasley, W. D.; and Harvey, W. D.: Experimental Results for a Flapped Natural-Laminar-Flow Airfoil with High Lift/Drag Ratio. NASA TM-85788, Apr. 1986.

13. Waggoner, Edgar G.: Computational Wing Design Studies Relating to Natural Laminar Flow. NASA CP-2413, Apr. 1986.

14. Morgan, Harry L., Jr.: High-Lift Flaps for Natural Laminar Flow Airfoils. NASA CP-2413, Apr. 1986.

15. Sewall, W. G.; McGhee, R. J.; Viken, J. K.; Waggoner, E. G.; Walker, B. S.; Millard, B. F.: Wind Tunnel Results for a High-Speed Natural Laminar Flow Airfoil Design for General Aviation Aircraft. NASA TM-87602, 1987.

16. Befus, J.; Nelson, R.; Latas, J., Sr.; and Ellis, D.: Flight Test Investigations of a Wing Designed for Natural Laminar Flow. SAE TP-871044, Apr. 1987.

17. Murri, Daniel G.; Jordan, Frank L.; Nelson, Randy; Davis, Patrick J.: Wind-Tunnel Investigation of a General Aviation Airplane Equipped with a High Aspect-Ratio, Natural Laminar-Flow Wing. SAE TP-871019, 1987.

18. McGhee, Robert J.; and Beasley, William D.: Wind Tunnel Results for a Modified 17-Percent-Thick Low-Speed Airfoil Section. NASA TP-1919, Nov. 1981.

19. Whitcomb, R. T.: Review of NASA Supercritical Airfoils ICAS Paper 74-10, Aug. 1974.

20. Dagenhart, J. R.: Amplified Crossflow Disturbances in the Laminar Boundary Layer on Swept Wings with Suction. NASA TP-1902, 1981.

21. Reed, H. L.: Wave Interactions in Swept Wing Flows. AIAA Paper 84-1678, 1984.

22. Reed, H. L.: Disturbance-Wave Interactions in Flows with Crossflow. AIAA Paper 85-0494, Jan. 1985.

23. Mack, L. M.: On the Stability of the Boundary Layer on a Transonic Swept Wing. AIAA 79-0264, Jan. 1979.

24. Nayfeh, A. H.: Effect of Streamwise Vortices on Tollmien-Schlichting Waves. Journal of Fluid Mechanics, vol. 107, 1981, pp. 441.

25. Poll, D. I. A.: Leading Edge Transition on Swept Wings. AGARD CP-224, 1977, pp. 21-1 to 21-11.

26. Nayfeh, A. H.: Influence of Görtler Vortices on Tollmien-Schlichting Waves. AIAA Paper 87-1206, Jun. 1987.

27. Hall, P.; Bennett, J.: Tayler-Görtler Instabilities of Tollmien-Schlichting Waves and Other Flows Governed by the Interactive Boundary-Layer Equations. Journal of Fluid Mechanics, vol. 171, 1986, pp. 441.

28. Mangalam, S. M.; Dagenhart, J. R.; and Kalburgi, V.: Influence of Suction and Curvature on the Growth of Görtler Vortices on an Airfoil. AIAA-87-0481, Jun. 1987.

29. Malik, M. R.: Wave Interaction in Three-Dimensional Boundary Layers. AIAA Paper 86-1129, 1986.

30. Herbert, T.; Morkovin, M. V.: Dialogue on Bridging Some Gaps in Stability and Transition Research. Laminar-Turbulent Transition, R. Eppler and H. Fasel, eds., Springer-Verlag, 1980.

31. Saric, William S.; and Reed, Helen L.: Three-Dimensional Stability of Boundary Layers. Proceeding Perspectives in Turbulence Symposium, Göttingen, West Germany, May 11-15, 1987.

32. Morkovin, M. V.: On the Many Faces of Transition Viscous Drag Reduction. C. S. Wells, ed., Plenum Publ., 1969.

33. Harvey, W. D.; and Pride, J. D.: The NASA Langley Laminar Flow Control Experiment. AIAA Paper 82-0567, Mar. 1982.

34. Pate, S. R.: Effects of Wind Tunnel Disturbances on Boundary-Layer Transition with Emphasis on Radiated Noise: A Review. AIAA Paper 80-0431, Mar. 1980.

35. Harvey, W. D.; and Bobbitt, P. J.: Some Anomalies Between Wind Tunnel and Flight Transition Results. AIAA Paper 81-1225, Jun. 1981.

36. Stainback, P. Calvin; Johnson, Charles B.; and Basnett, Constance B.: Preliminary Measurements of Velocity, Density, and Total Temperature Fluctuations in Compressible Subsonic Flow. AIAA 83-0384, Jan. 1985.

37. Gray, W. E.: Transition in Flight on a Laminar-Flow Wing of Low Waviness (King Cobra). R.A.E. Report 2364, Mar. 1950.

38. Gray, W. E.; and Fullam, P. W. J.: Comparison of Flight and Wind Tunnel Measurements of Transition on a Highly Finished Wing (King Cobra). R.A.E. Report 2383, Jun. 1950.

39. Spee, B. M.: Investigations on the Transonic Flow Around Airfoils. NLR TR-6912225, Mar. 1971.

40. Carmichael, B. H.: Surface Waviness Criteria for Swept and Unswept Laminar Suction Wings. Northrop Rpt. NOR-59-438, 1959.

41. Carmichael, B. H.: Surface Imperfection Experiments on a Swept Laminar Suction Wing. Northrop Rpt. BLC-124, NOR-59-454, 1959.

42. Newman, P. A.; Kemp, W. B.; and Garriz, J. A.: Wall Interference Assessment and Correlations. Transonic Symposium: Theory, Application, and Experiment. NASA CP-3020, 1989, pp. 817-852.

43. Pfenninger, W.; Gross, Lloyd; and Bacon, John W., Jr.: Experiments on a 30° Swept 12-Percent Thick Symmetrical Laminar Suction Wing in the 5- by 7-Foot Michigan Tunnel. Rep. NAI-57-317 (BLC-93), Northrop Aircraft Inc., Feb. 1957.

44. Newman, Perry A.; Anderson, E. Clay; and Peterson, John B, Jr.: Aerodynamic Design of the Contoured Wind Tunnel Liner for the NASA Supercritical Laminar Flow Control, Swept Wing Experiment. NASA TP-2335, Sept. 1984.

45. Dagenhart, J. Ray; and Stack, John P.: Boundary-Layer Transition Detection Using Flush-Mounted Hot-Film Gages and Semiconductor Dynamic Pressure Transducers. AIAA Paper 82-0593, Mar. 1982.

46. Stack, John P.; Mangalam, Siva M.; and Kalburgi, Vijay: The Phase Reversal Phenomena at Flow Separation and Reattachment. AIAA 88-0408, Jan. 1988.

47. Bobbitt, P. J.: Instrumentation Advances for Transonic Testing. Transonic Symposium, NASA Langley Research Center, Hampton, VA, April 19-21, 1988.

48. Harris, Charles D.; and Brooks, Cuyler, W.: Modifications to the Langley 8-Foot Transonic Pressure Tunnel for the Laminar Flow Control Experiment. NASA TM-4032, 1988.

49. Lee, J. D.; Gregorek, G. M.; and Korkan, K. D.: Testing Techniques and Interference Evaluation in the OSU Transonic Airfoil Facility. AIAA 78-1118, Jul. 1978.

50. Bauer, F.; Garabedian, P.; Korn, D.; and Jameson, A.: Supercritical Wing Sections II. Volume 108 of Lecture Notes in Economics and Mathematical Systems, Springer-Verlag, 1975.

51. Lachman, G. V. (editor): Boundary Layer and Flow Control. Vol. II, Pergamon Press, 1961.

52. Pfenninger, W.; and Growth, E.: Low Drag Boundary Layer Suction Experiments in Flight on a Wing Glove of an F-94A Airplane with Suction Through a Large Number of Fine Slots. Boundary Layer and Flow Control, vol. 2, G. V. Lachmann, ed., 1961, pp. 981-999.

53. Fowell, L. R.; and Antonatos, P. P.: Laminar Flow Control Flight Test Results, Some Results from the X-21A Program. Recent Developments in Boundary Layer Research, Part IV, May 1965. AGARDograph 97, pp. 1-76.

54. Maddalon, Dal V.: Design and Fabrication of Large Suction Panels with Perforated Surfaces for Laminar Flow Control Testing in a Transonic Wind Tunnel. NASA TM-89011, Aug. 1986.

55. Whites, R. C.; Sudderth, R. W.; and Wheldon, W. G.: Laminar Flow Control on the X-21. Astronautics and Aeronautics, Jul. 1966, pp. 38-43.

56. Goradia, S. H.; Bobbitt, P. J.; Ferris, J. C.; and Harvey, W. D.: Theoretical Investigations and Correlative Studies for NLF, HLFC, and LFC Swept Wings at Subsonic, Transonic, and Supersonic Speeds. SAE Paper 871861, Oct. 1987.

57. Van Ingen, J. L.; Blom, J. J. H.; and Goei, J. H.: Design Studies of Thick Laminar Flow Airfoils for Low-Speed Flight Employing Turbulent Boundary-Layer Suction Over the Rear Part. AGARD CP-365, May 1984.

58. Klebanoff, P. S.; and Tidstron, K. D.: Evolution of Amplified Waves Leading to Transition in a Boundary Layer with Zero Pressure Gradient. NASA TN D-195, 1958.

59. Srokowski, A. J.; and Orszag, S. A.: Mass Flow Requirements for LFC Wing Design. AIAA Paper 77-1222, Aug. 1977.

60. Malik, M. R.; and Orszag, S. A.: Efficient Computation of the Stability of Three-Dimensional Compressible Boundary Layers. AIAA Paper 81-1277, Jun. 1981.

61. Mack, L. M.: Transition Prediction and Linear Stability Theory. AGARD CP-224, Jan. 1970.

62. Berry, Scott A.; Dagenhart, J. Ray; Viken, Jeffery K.; and Yeaton, Robert B.: Boundary-Layer Stability Analysis of NLF and LFC Experimental Data at Subsonic and Transonic Speeds. SAE TPS-871859, Oct. 1987.

63. Vijgen, P. M. H. W.; Dodbele, S. S.; Pfenninger, W.; and Holmes, B. T.: Analysis of Wind Tunnel Boundary-Layer Transition Experiments on Axisymmetric Bodies at Transonic Speeds Using Compressible Boundary-Layer Stability Theory. AIAA 88-0008, Jan. 1988.

64. Hefner, J. N.; and Bushnell, D. M.: Application of Stability Theory to Laminar Flow Control. AIAA Paper 79-1493, Jul. 1979.

65. Runyan, L. J.; Navran, B. H.; and Rozendaal, R. A.: F-111 Natural Laminar Flow Glove Flight Test Data Analysis and Boundary Layer Stability Analysis. NASA CR-166051, 1984.

66. Runyan, L. James: Boundary Layer Stability Analysis of a Natural Laminar Flow Glove on the F-111 Tact Airplane. Symposium on Viscous Drag Reduction, Dallas, Texas, Nov. 7-8, 1979.

67. Croom, Cynthia C.; Manuel, Gregory S.; and Stack, John P.: In-Flight Detection of Tollmien-Schlichting Instabilities in Laminar Flow. SAE Paper 871016, Apr. 1987.

68. Boeing Commercial Airplane Company: Flight Survey of the 757 Wing Noise Field and Its Effects on Laminar Boundary Layer Transition. Vols. I and II. NASA CR-178216, 1987.

69. Rozendaal, R. A.: Natural Laminar Flow Flight Experiments on a Swept Wing Business Jet - Boundary Layer Stability Analysis. NASA CR-3975, May 1986.

70. Rozendaal, R. A.: Variable-Sweep Transition Flight Experiment (VSTFE) Stability Code Development and Clean-Up Glove Data Analysis. NASA CP-2487, March 1987.

71. Mack, L. M.: Transition and Laminar Instability. JPL Publication 77-15, 1977.

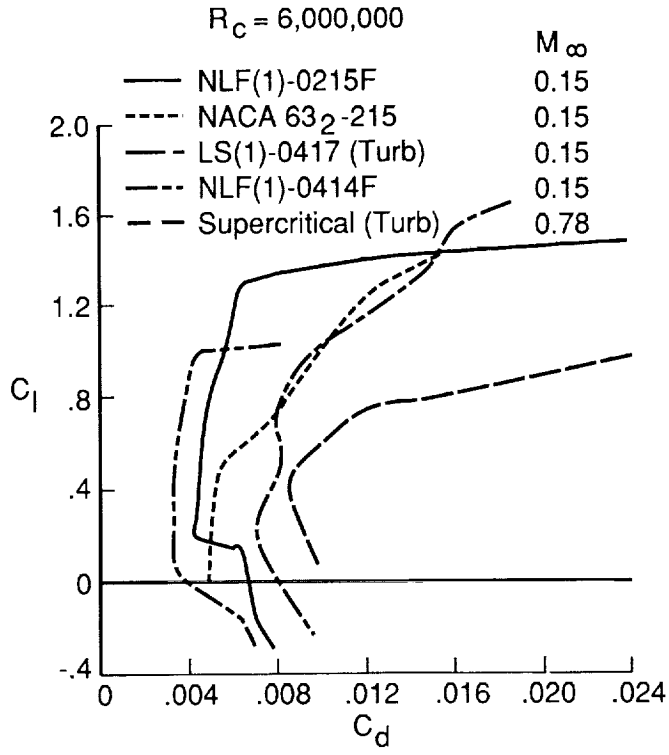

Figure 1. Comparison of drag polars on airfoils at low and high speeds with and without flap deflection.

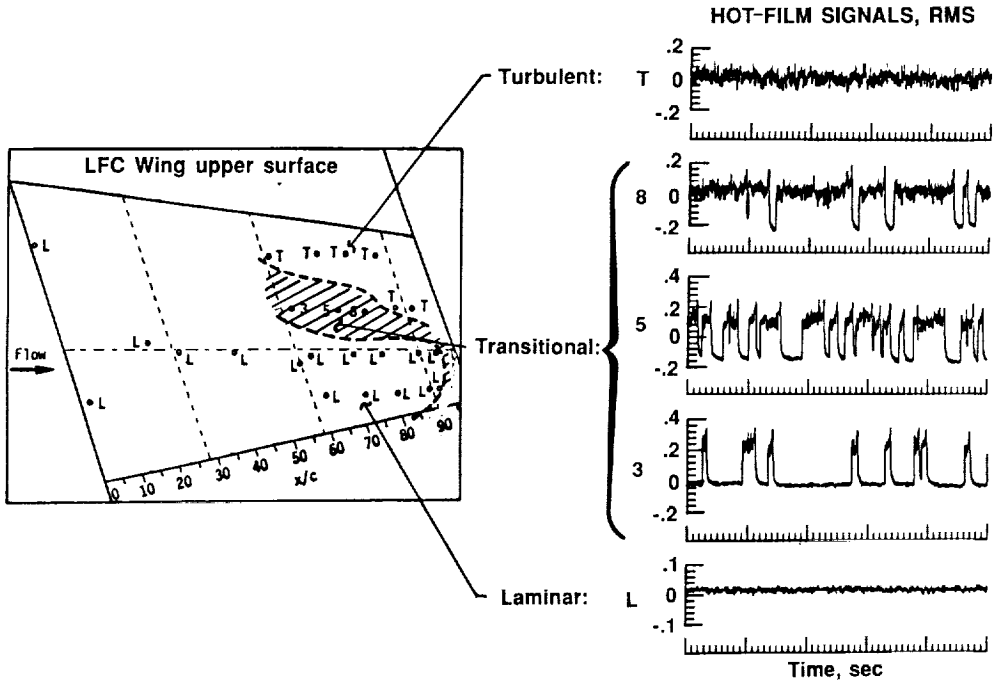

Figure 2. An example of flush-mounted surface hot-film gage locations, RMS output signals, and laminar pattern.

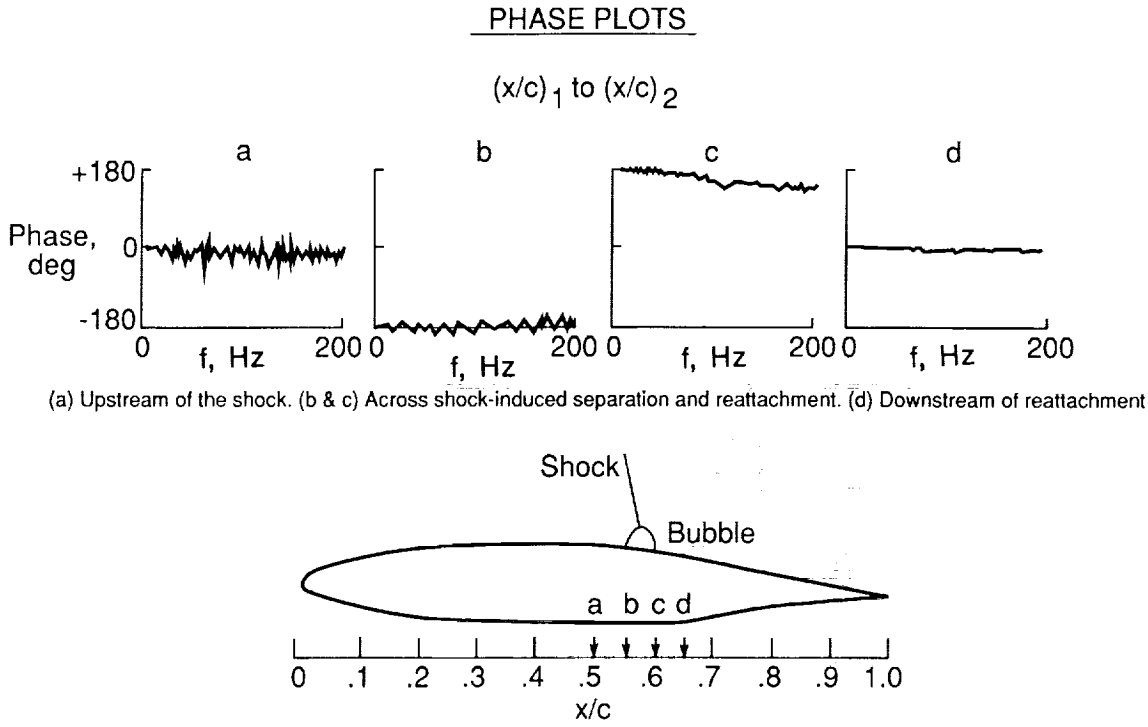

(a) Upstream of the shock. (b & c) Across shock-induced separation and reattachment. (d) Downstream of reattachment

Figure 3. Example of multielement dynamic shear stress sensor detection of shock-induced separation by phase reversal.

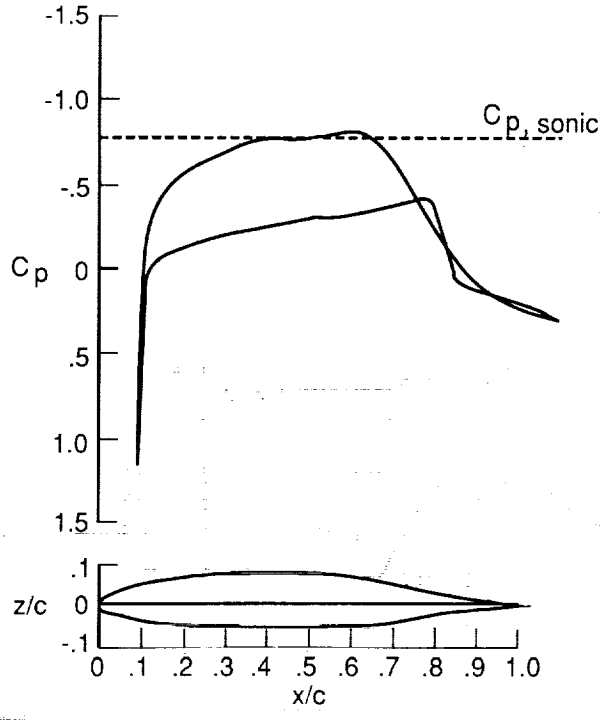

Figure 4. Design theoretical pressure distribution and geometry for HSNLF(1)-0213 airfoil. $M_\infty = .7$, $C_L = .26$, $R_c = 11 \times 10^6$, $\Lambda = 0°$.

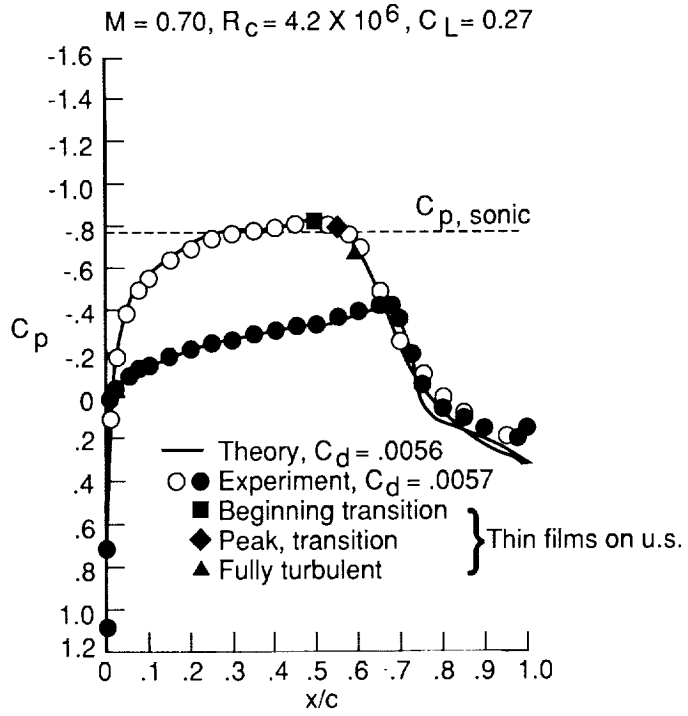

Figure 5. Comparison of experimental and theoretical pressure distributions for HSNLF(1)-0213 airfoil.

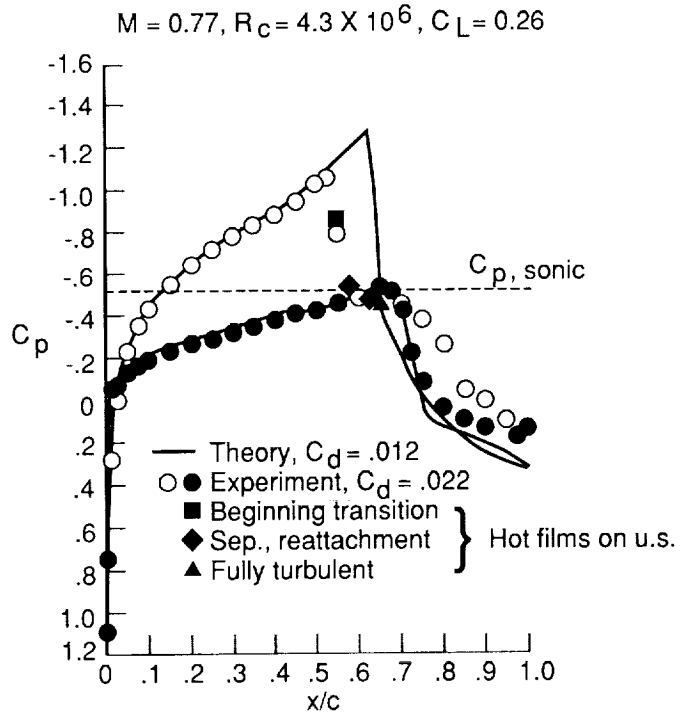

Figure 6. Comparison of experimental and theoretical pressure distributions for HSNLF(1)-0213 airfoil at off-design conditions.

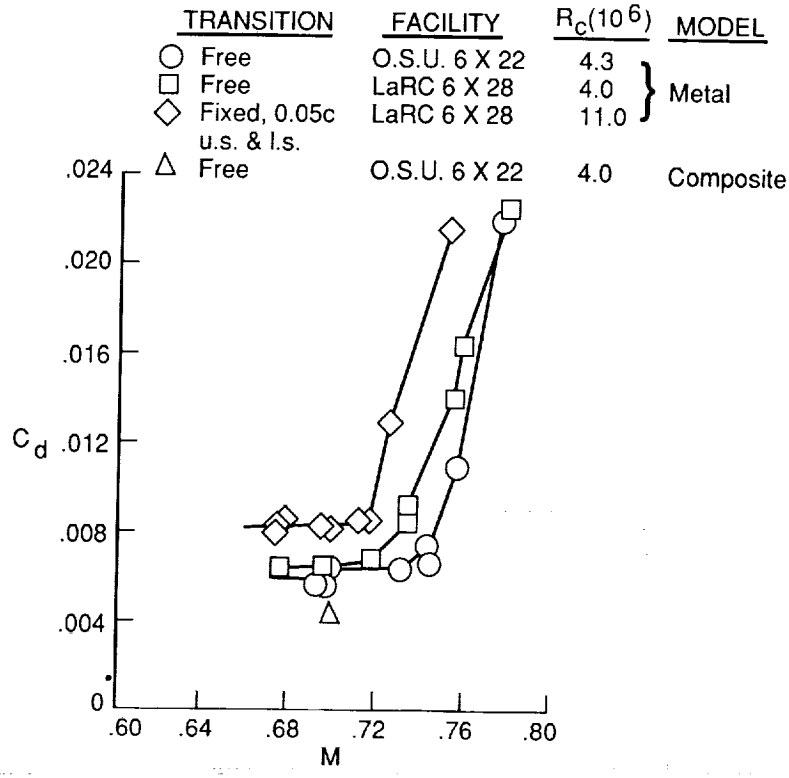

Figure 7. Effect of Mach number on drag coefficient for the HSNLF(1)-0213 airfoil in two different wind tunnels at zero angle of attack.

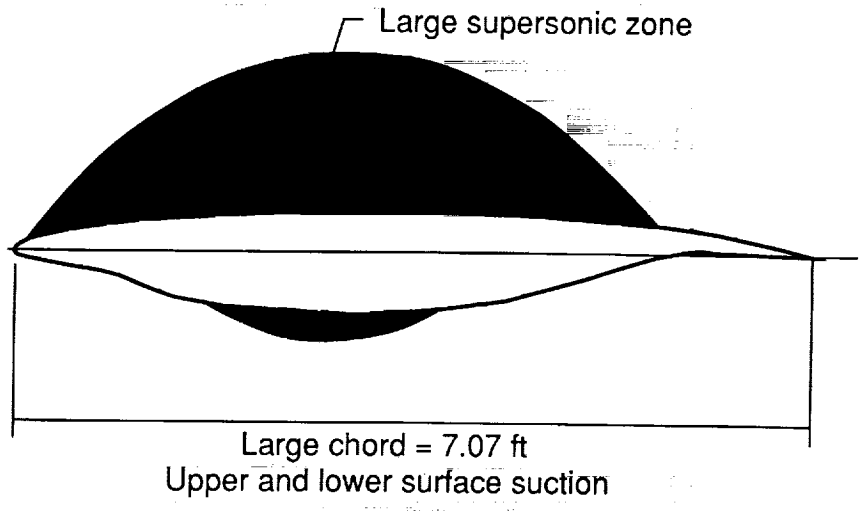

FREE-STREAM DESIGN CONDITIONS	DESIGN CONDITIONS NORMAL TO LEADING EDGE
$M_\infty = 0.82$	$M_\infty = 0.755$
$\Lambda = 23^o$	$c_N = 6.508$ ft
$c = 7.07$ ft	$R_{c,N} = 16.9 \times 10^6$
$R_c = 20 \times 10^6$	$(t/c)_N = 13.0$ percent
$C_l = 0.47$	$C_{l,N} = 0.55$

Figure 8. Schematic of swept SCLFC(1)-0513F airfoil, sonic zones, and design conditions.

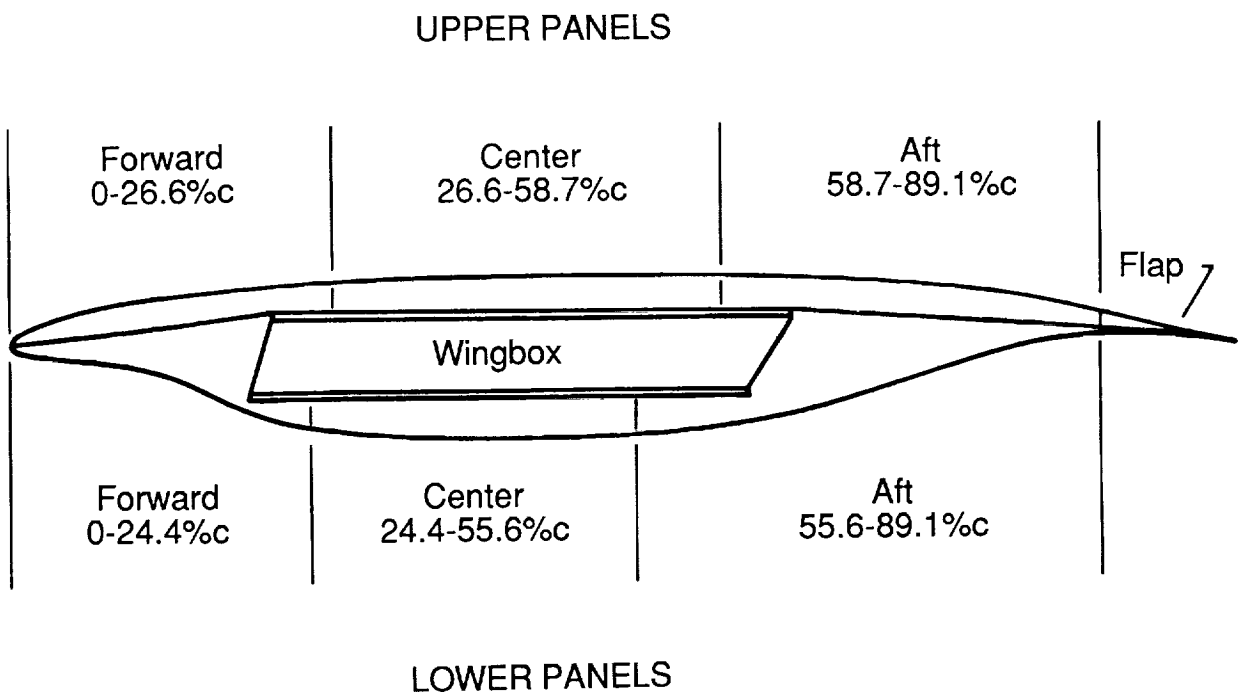

Figure 9. Schematic of SCLFC(1)-0513F airfoil wingbox and suction panel assembly.

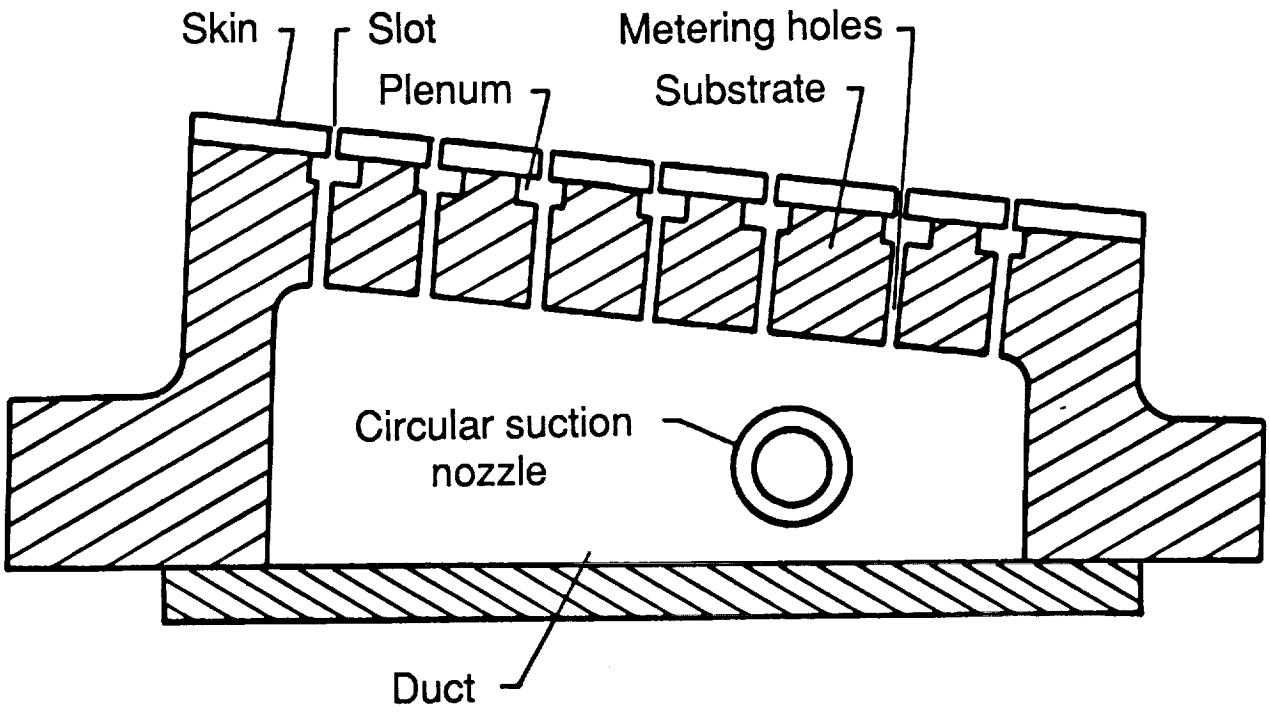

Figure 10. Schematic section of slotted suction surface panel concept.

(a) View looking downstream at model leading edge and upper surface.

Figure 11. Photograph of swept supercritical LFC airfoil model and contoured wall liner in the Langley 8-Foot Transonic Pressure Tunnel.

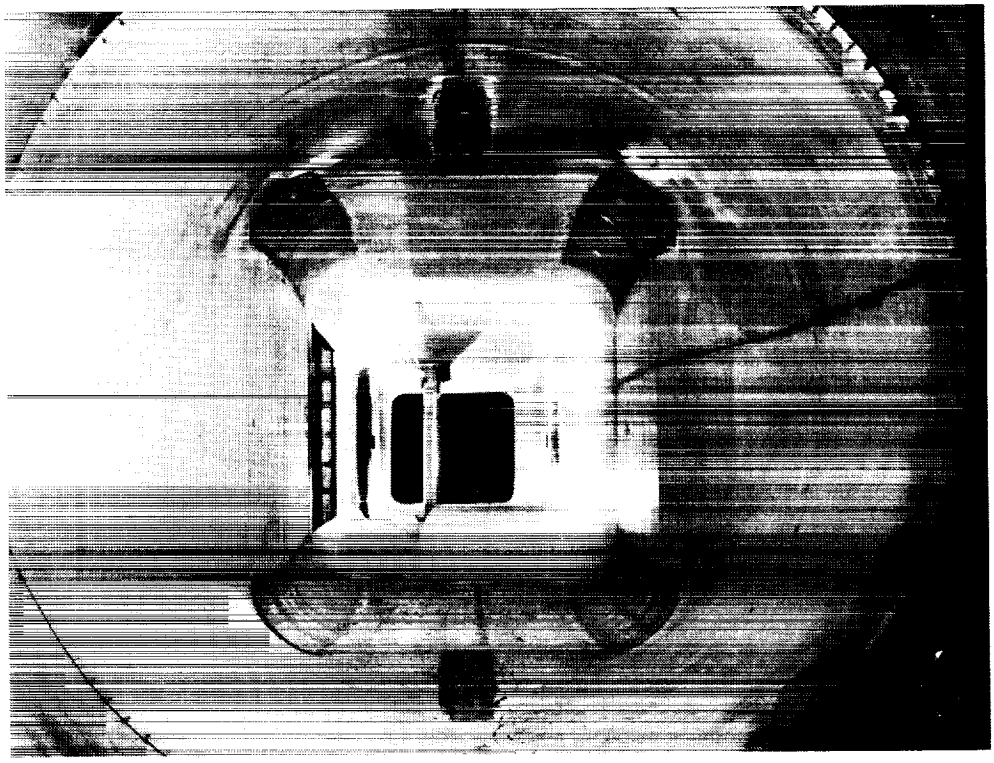

(b) View looking upstream at model trailing edge and liner step.

Figure 11. Concluded.

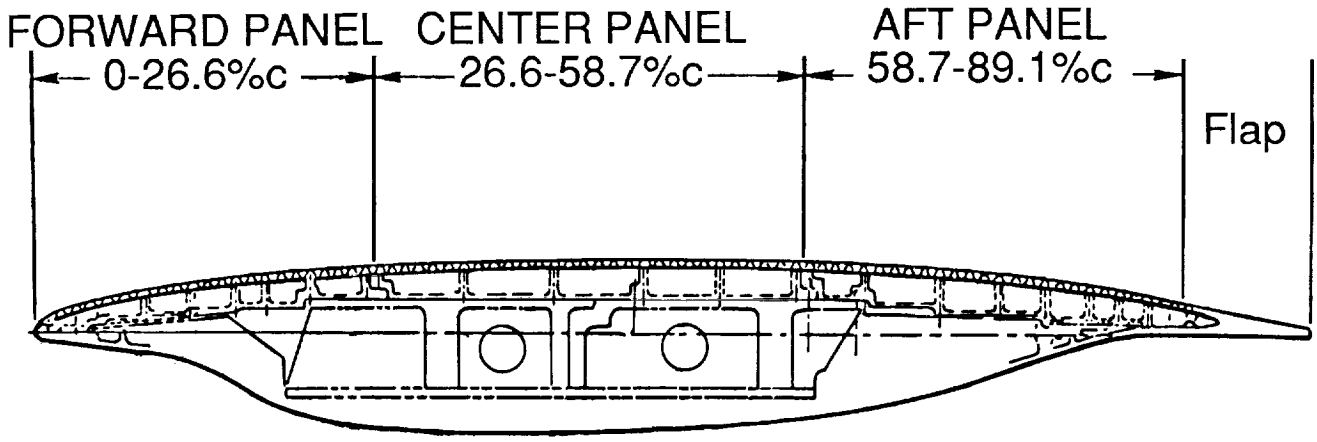

Figure 12. Schematic of LFC airfoil model with porous upper surface panels.

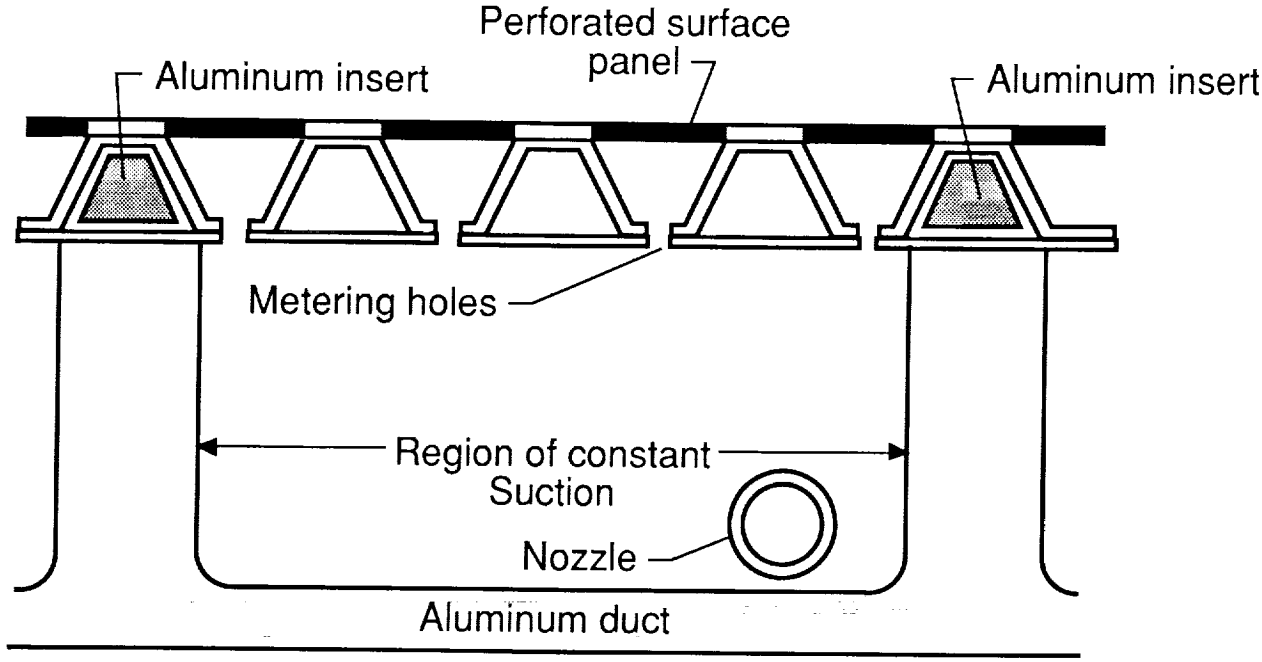

Figure 13. Schematic section of perforated suction surface panel concept.

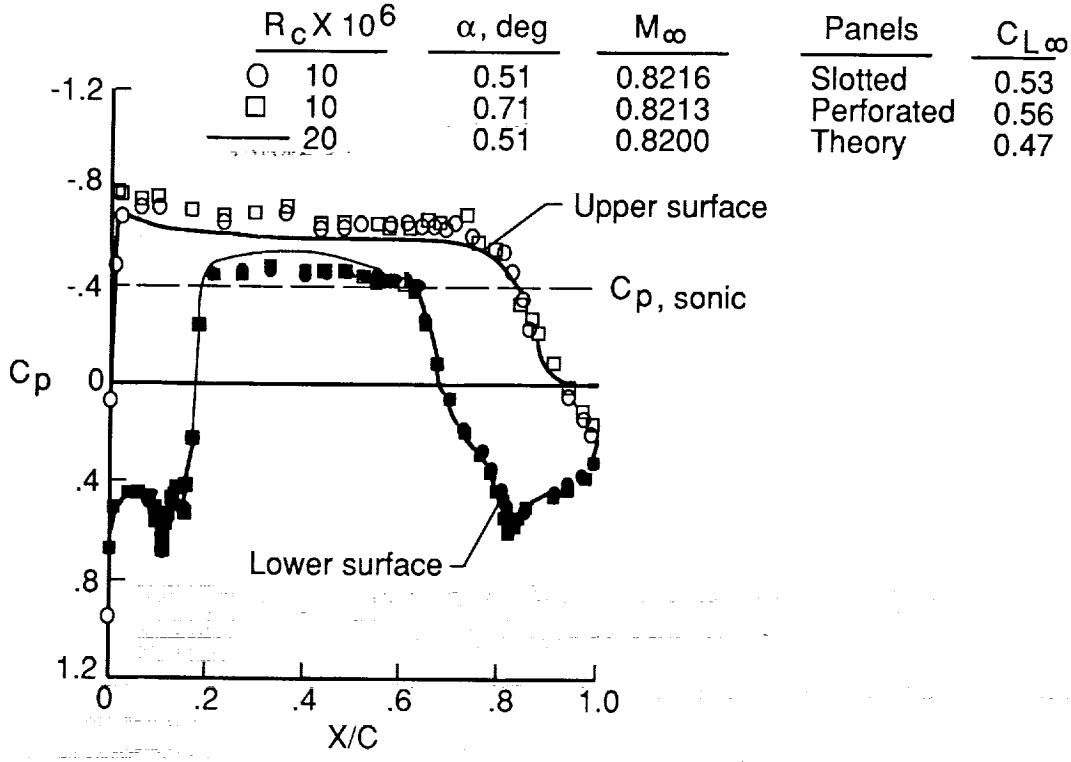

Figure 14. Comparison of experimental and theoretical pressure distributions for SCLFC(1)-0513F airfoil with slotted and perforated surface.

$R_c = 10 \times 10^6$.

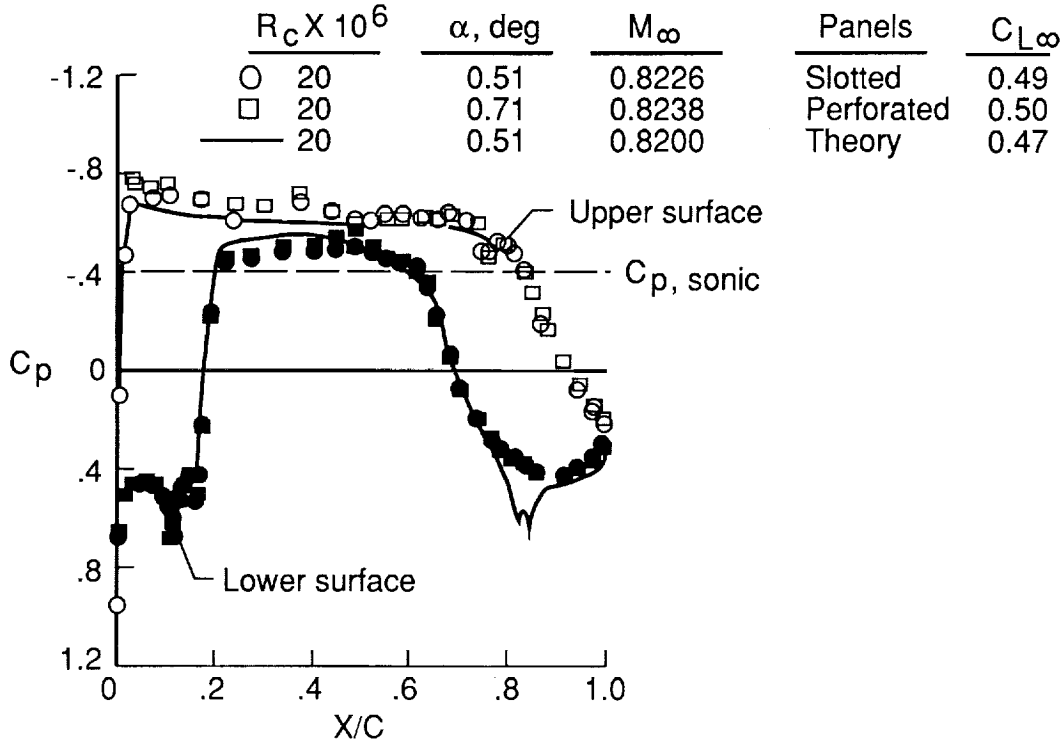

Figure 15. Comparison of experimental and theoretical pressure distributions for SCLFC(1)-0513F airfoil with slotted and perforated surfaces. $R_c = 20 \times 10^6$.

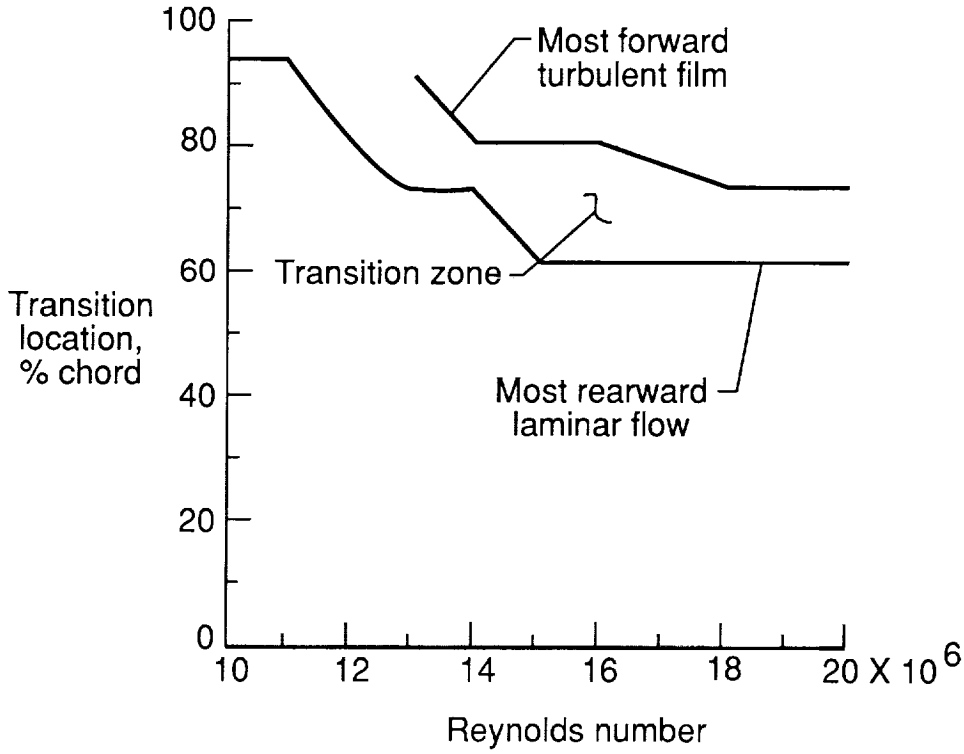

Figure 16. Measured transition location on upper surface of slotted SCLFC(1)-0513F airfoil. $M_\infty = 0.82$.

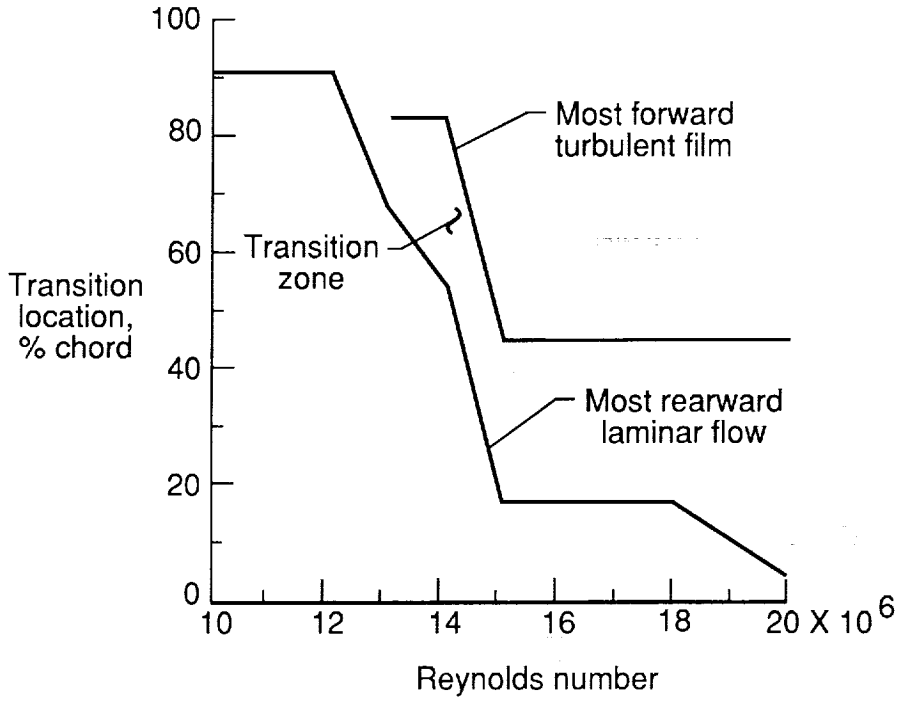

Figure 17. Measured transition location on lower surface of slotted SCLFC(1)-0513F airfoil. M = 0.82.

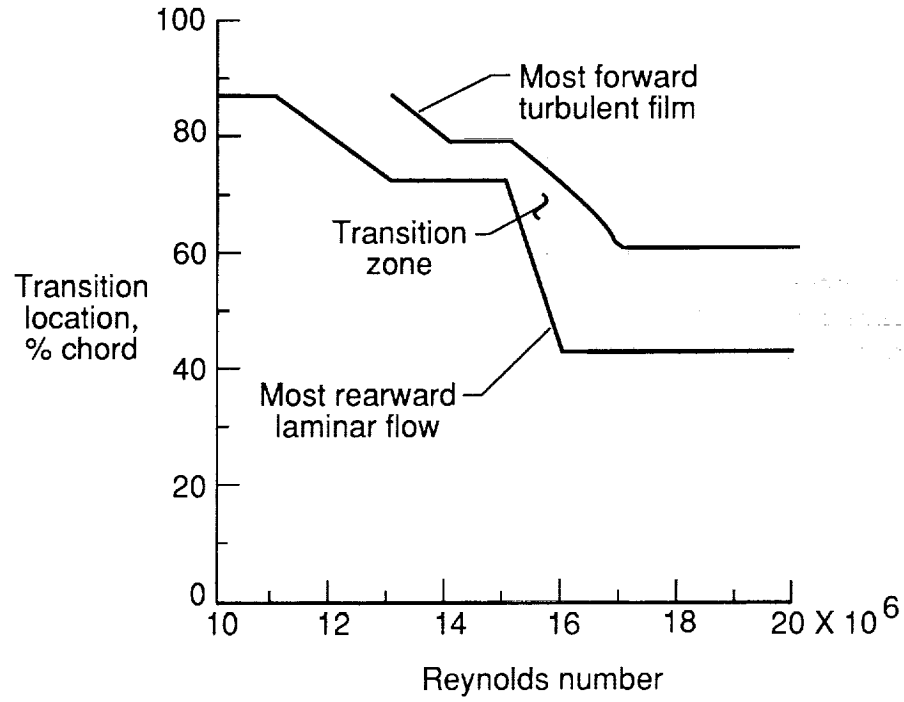

Figure 18. Measured transition location on upper surface of perforated SCLFC(1)-0513F airfoil. M_∞ = 0.82.

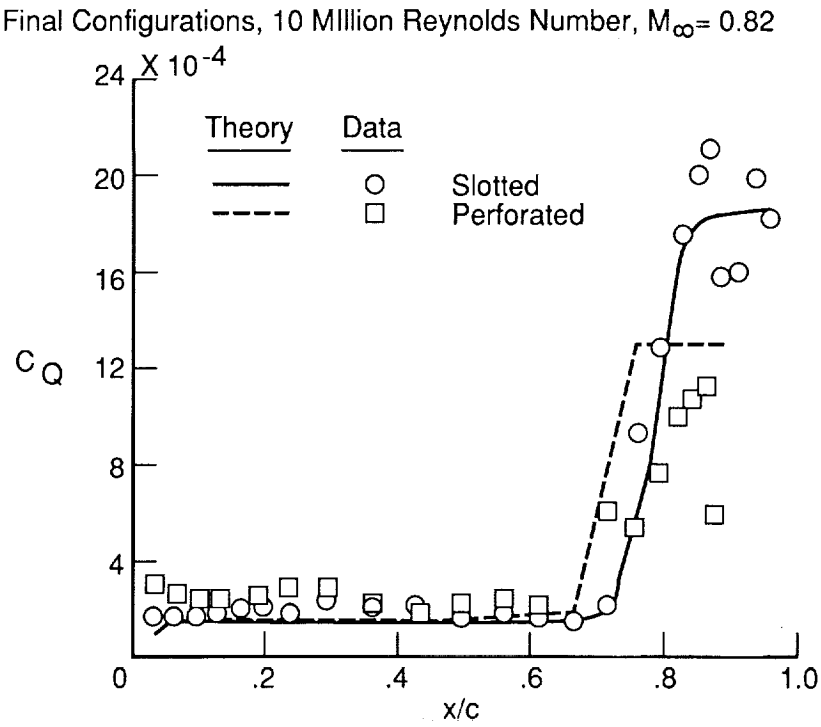

Figure 19. Comparison of experimental and theoretical suction distributions on upper surface of slotted and perforated SCLFC(1)-0513F airfoil models. M_∞ = 0.82, R_c = 10 x 10^6.

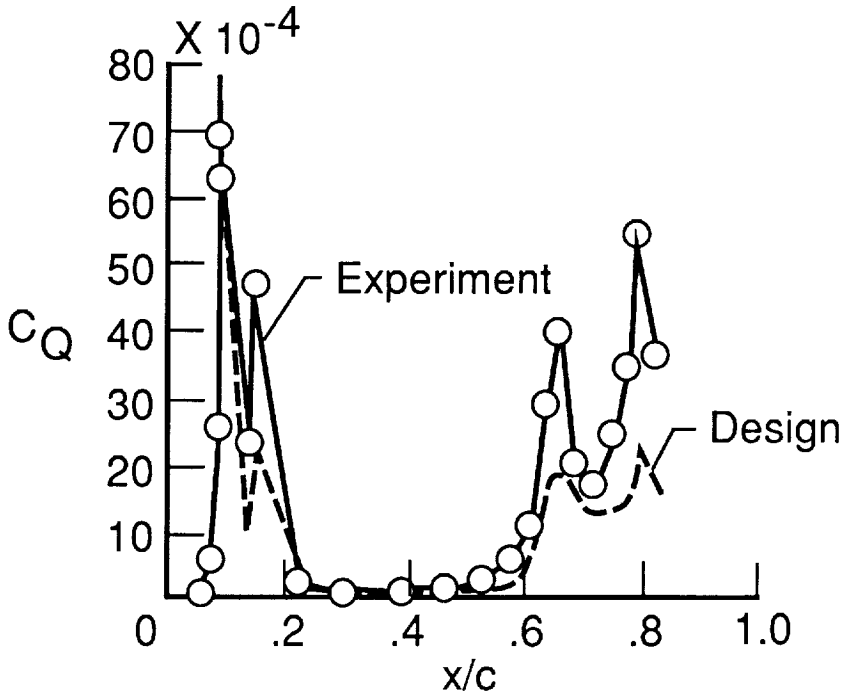

Figure 20. Comparison of experimental and theoretical suction distributions on the lower surface of slotted SCLFC(1)-0513 airfoil model. M_∞ = 0.82, R_c = 10 x 10^6.

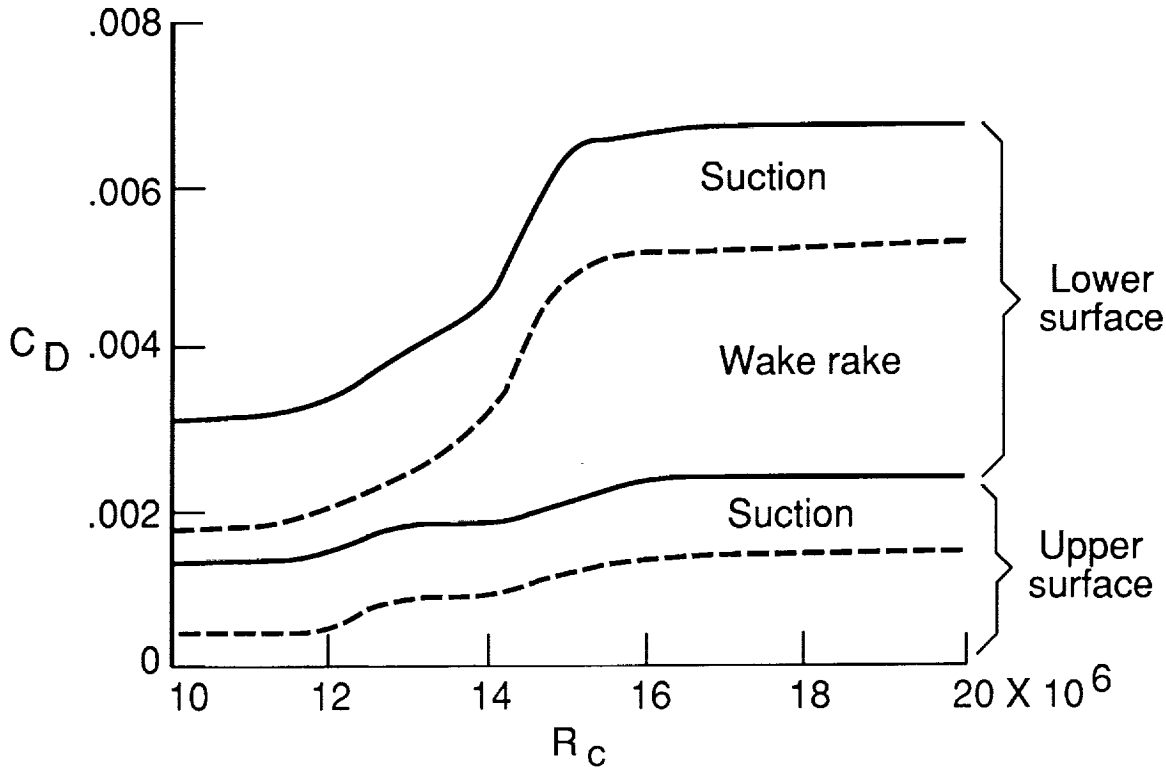

Figure 21. Measured variation of drag with chord Reynolds number on SCLFC(1)-0513F airfoil with slotted suction surface. M_∞ = 0.82.

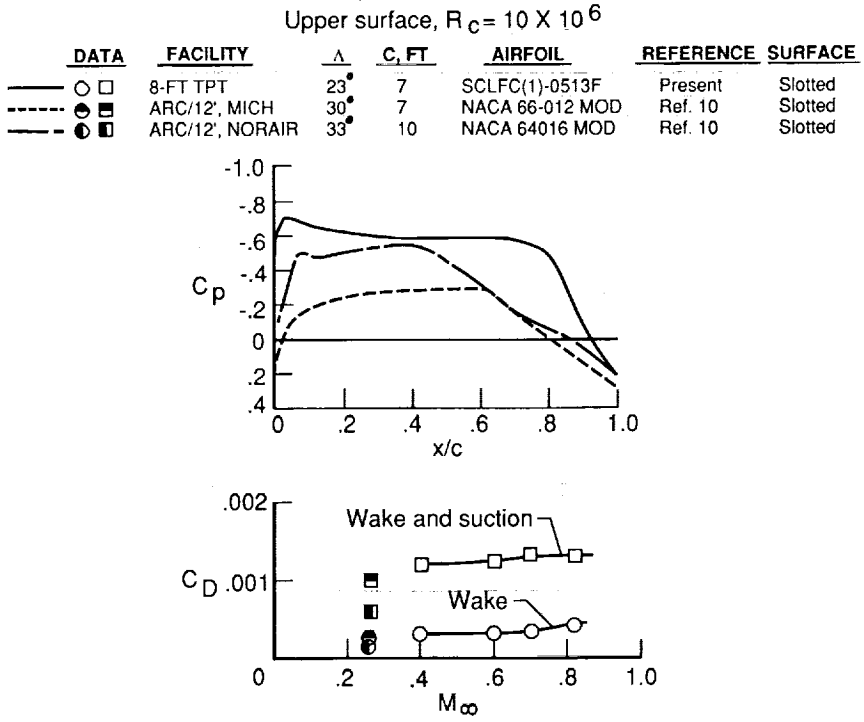

Figure 22. Comparison of measured pressure distributions and total drag for upper surface only on LFC wind tunnel models over speed range.

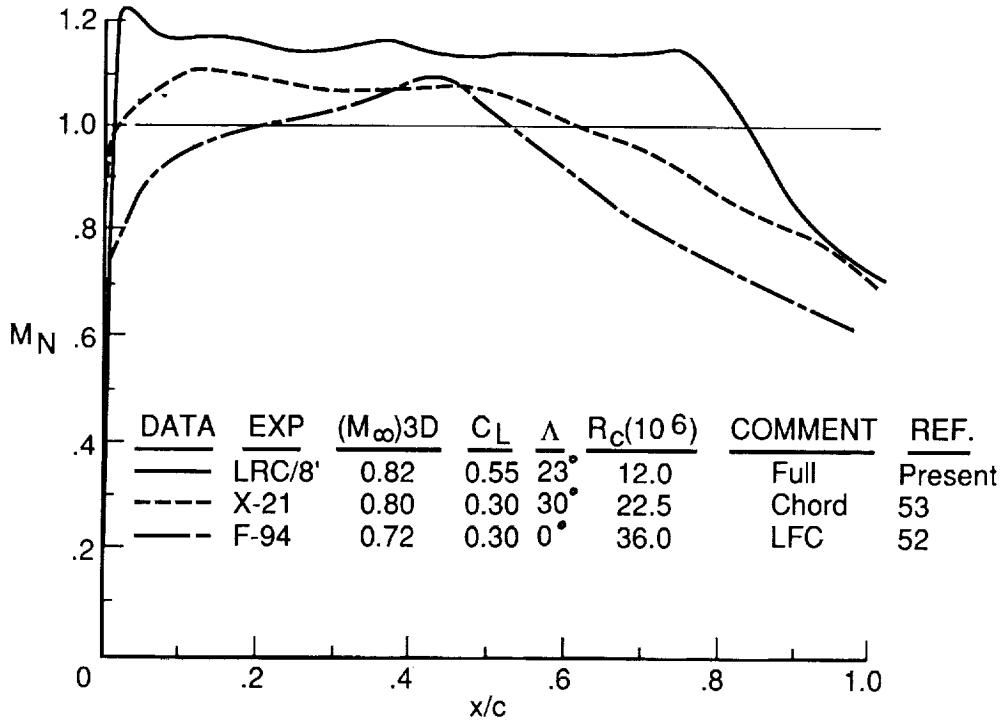

Figure 23. Comparison of measured local Mach number distributions on upper surface of wind tunnel and flight LFC wings at transonic speeds.

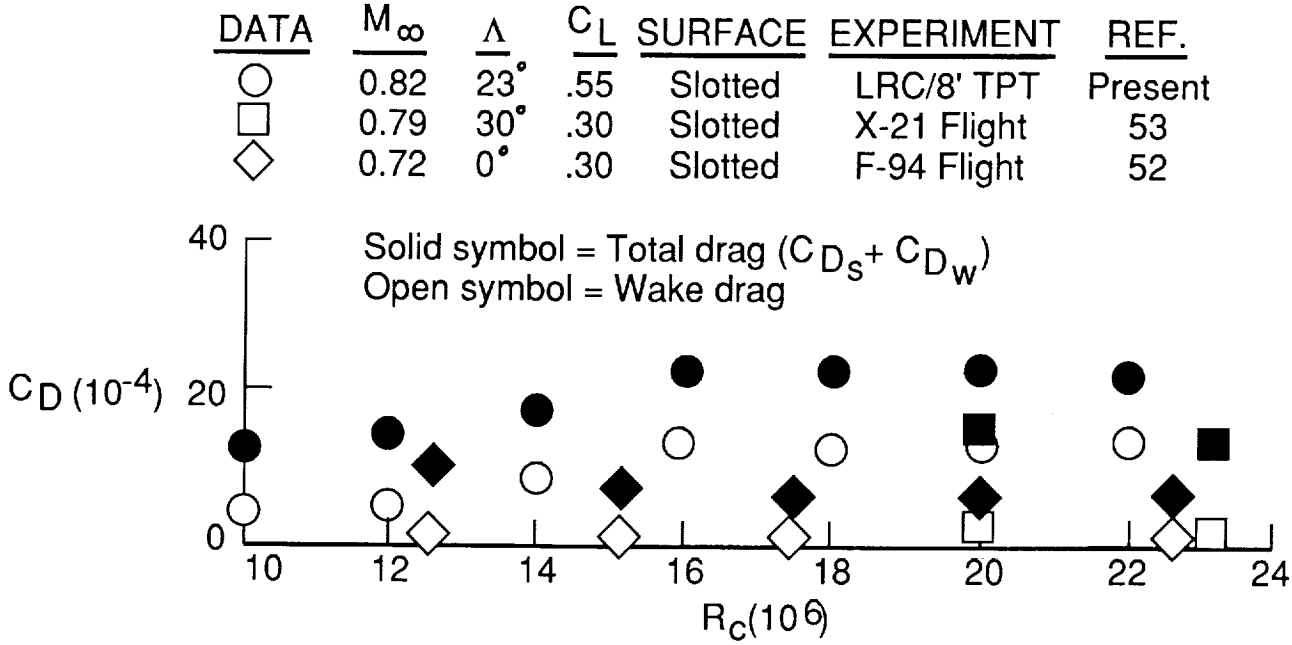

Figure 24. Comparison of drag coefficients for upper surface of swept and unswept transonic suction wings.

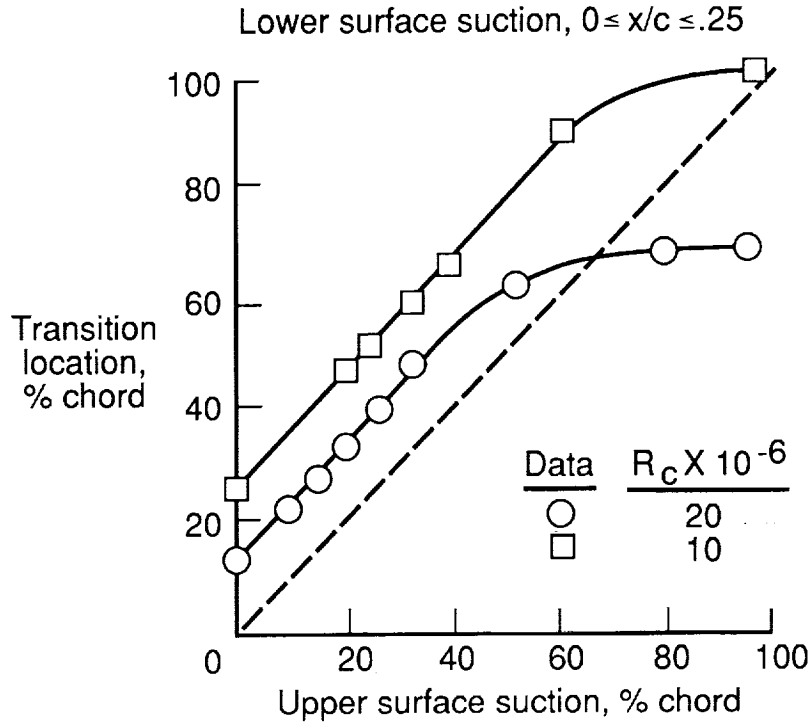

Figure 25. Variation of measured transition for simulated hybrid LFC on swept SCLFC(1)-0513F airfoil with slotted upper surface.

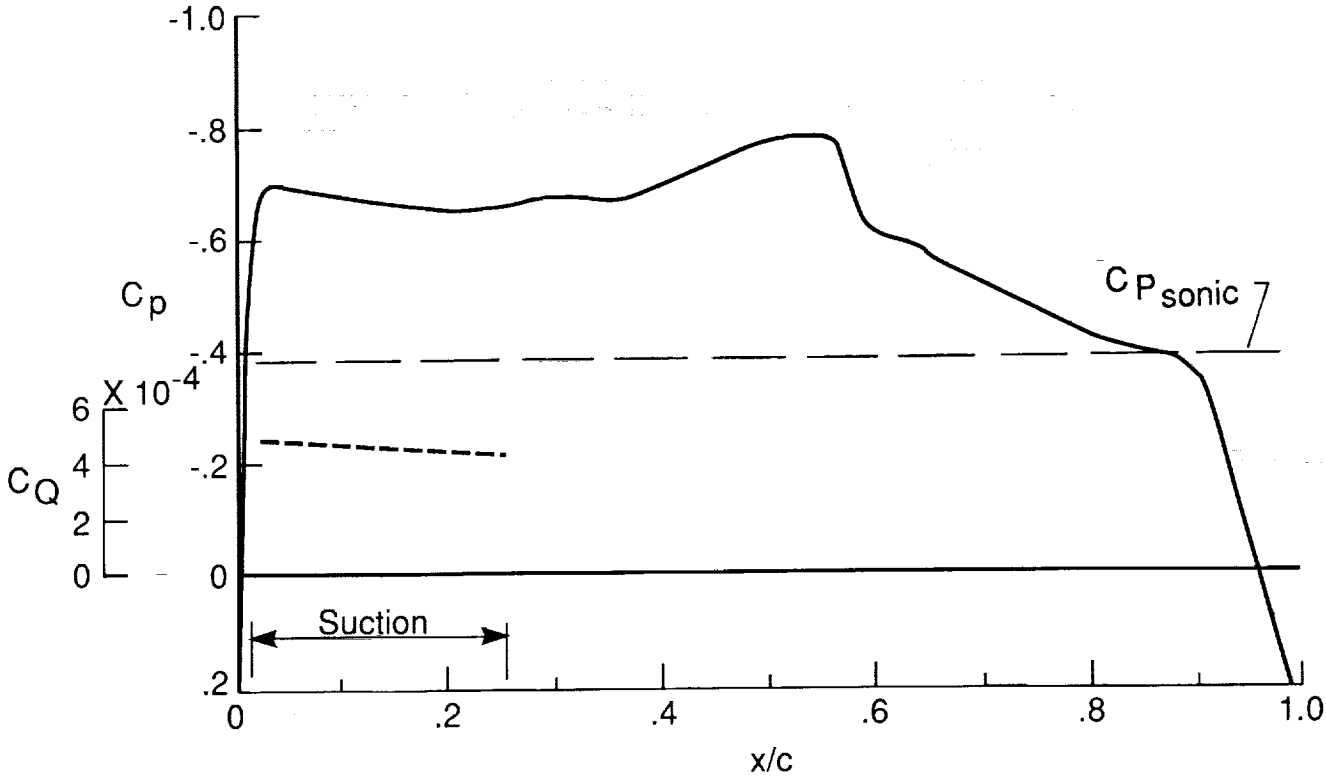

Figure 26. Design theoretical pressure and suction distributions on upper surface of hybrid LFC airfoil. M_∞ = 0.811, C_L = 0.47, R_c = 15 x 10^6, Λ = 23°.

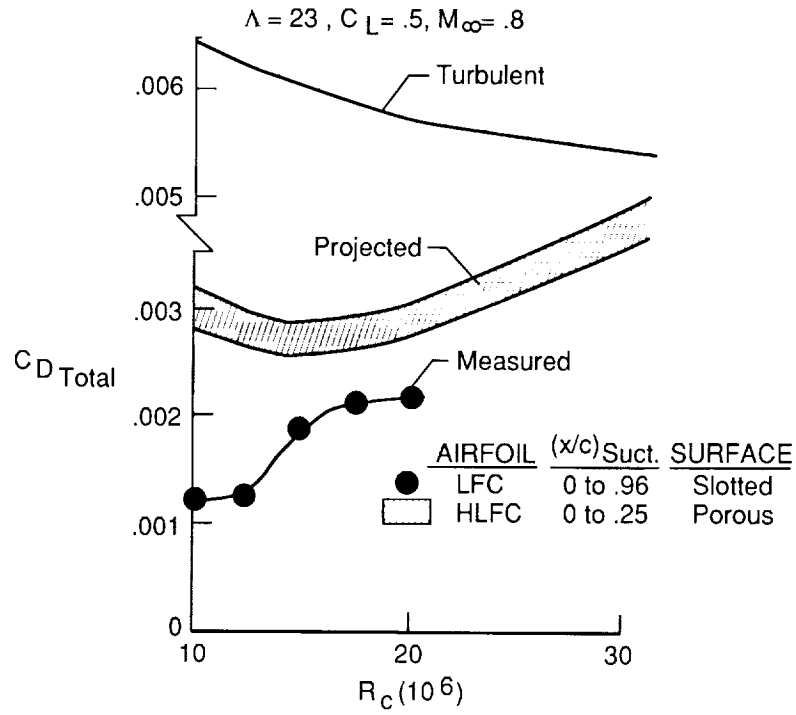

Figure 27. Measured and projected effect of suction extent on drag for LFC and HLFC airfoil upper surface.

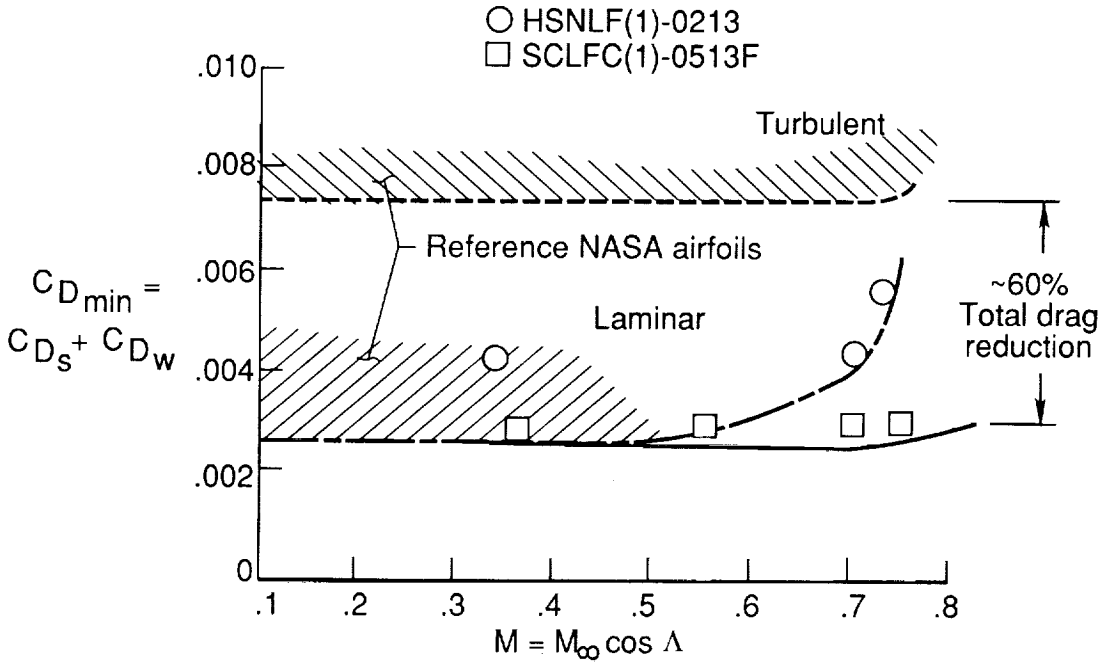

Figure 28. Comparison of measured minimum drag on NASA advanced low-drag airfoils, with and without suction, at transonic speeds with previous results (hatched areas).

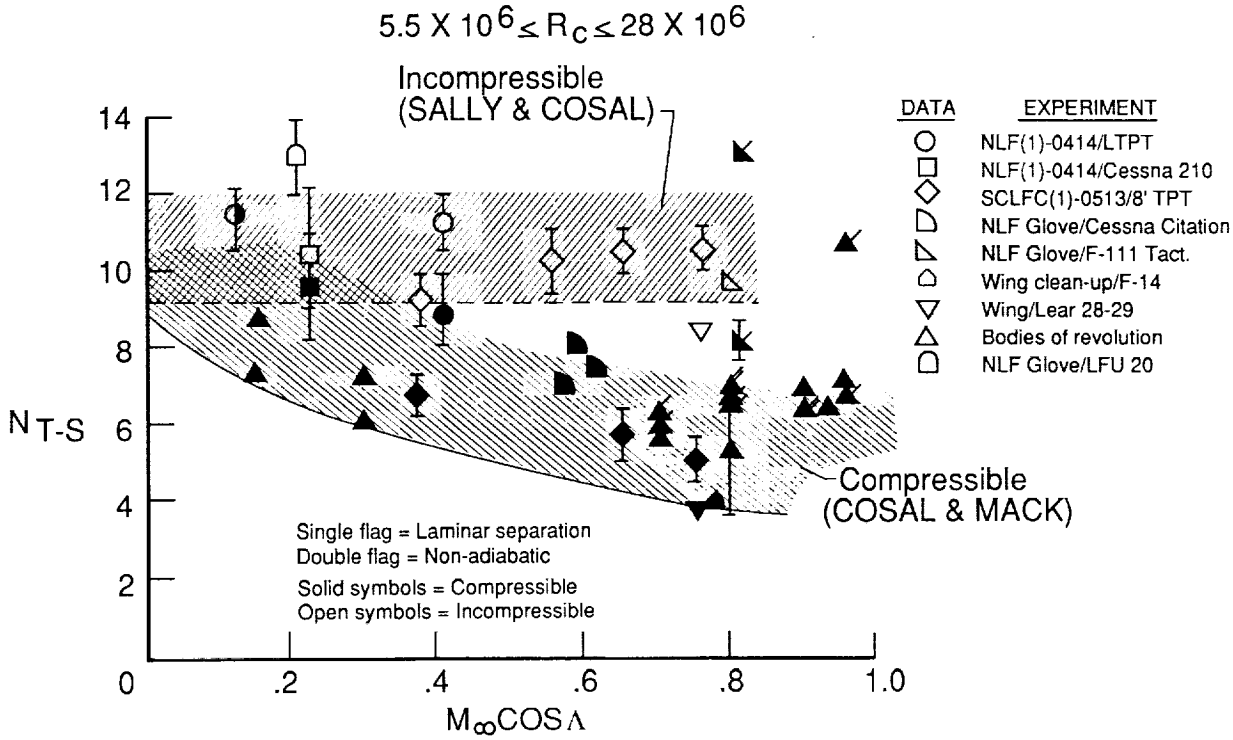

Figure 29. Minimum allowable Tollmien-Schlichting disturbance amplification N-factors at measured transition.

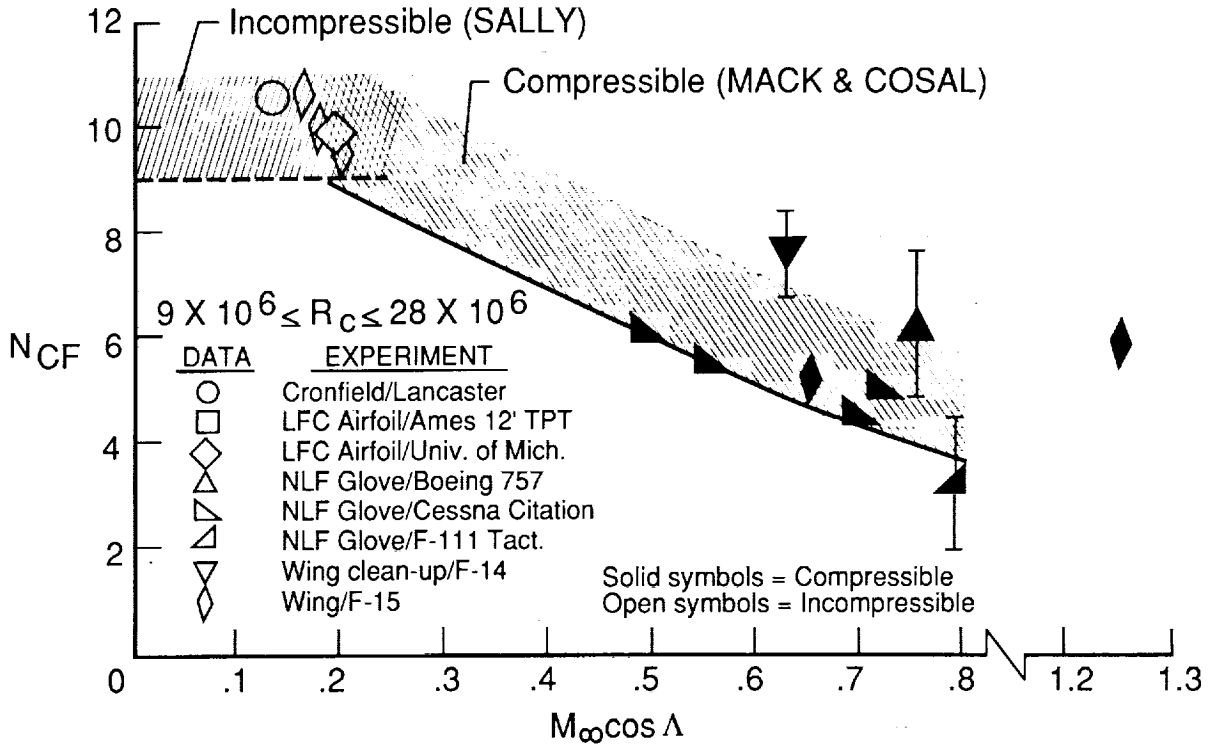

Figure 30. Minimum allowable crossflow disturbance amplification N-factors at measured transition.

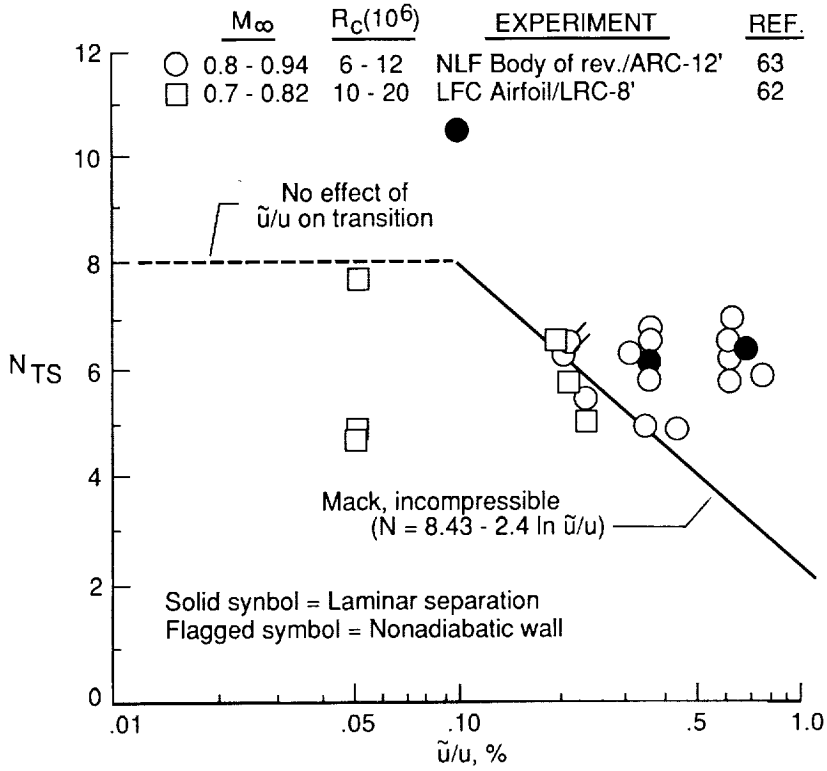

Figure 31. Variation of compressible N-factors at transition with turbulence level.